EGS-relevant review of orebody structures

CHPM2030 Deliverable D1.3

Version: December 2016

CHPM2030 DELIVERABLE D1.3

EGS-RELEVANT REVIEW OF OREBODY STRUCTURES

Summary:

This document provides the results of laboratory investigations on ore samples wich represent the study sites of the CHPM2030 project, completed with samples from other ore types. The results are evaluated with a relevancy to the CHPM technology. The methodology for rock stress and strength measurements is also described. These measurements will be carried out in the frame of WP2 and will complete the EGS relevant properties of different ore body types determined in the recent study.

Authors:

Norbert Németh, János Földessy, Éva Hartai, Ferenc Mádai, Ferenc Kristály, Ferenc Móricz, Ákos Debreczeni, Anett Kiss *(University of Miskolc)*
Máté Osvald, János Szanyi *(University of Szeged)*

Table of contents

1   Executive summary

In the provisioned CHPM technology an enhanced geothermal system would be established on a deep metal-bearing geological formation, which would be conducted in a way that the co-production of energy and metals could be possible. The aim of the recent study is to evaluate the mineralogical, petrographical and geochemical characteristics of different ore types which are relevant to this technology, and provide a methodological framework to the rock stress and strength measurements which will be carried out in the following phase of the project, within WP2, Task 2.1.

The examined samples were collected from the study sites: the Cornubian Ore Field (SW England), the Banatitic Magmatic and Metallogenic Belt (Romania), the three mining districts of Sweden (Bergslagen, Skellefte and Northern Norrbotten) and the Iberian Pyrite Belt (Portugal); and were completed by further samples from different ore types in Hungary.

The following laboratory examinations were carried out on the samples: X-ray diffraction, X-ray fluorescence spectrometry, rock and ore microscopy, and electron microprobe and EDX analysis. The samples were classified into six texture groups, based on the microscopic examinations. The main characteristics of the samples are discussed by grouping them into the represented ore types.

Although there are several limitations for drawing general, CHPM-relevant conclusions from the examination results, they will serve as a good base and practical input for the following phases of the project, mainly for the planning and interpretation of the leaching and the petrophysical tests.

2 Introduction

2.1 Objectives and role of the CHPM2030 project

The strategic objective of the CHPM2030 project is to develop a novel technological solution (Combined Heat, Power and Metal extraction from ultra deep ore bodies), which will help reducing Europe's dependency on the import of metals and fossil fuels, and at the same time, lower the environmental impact of the energy supply.

In the envisioned technology, an Enhanced Geothermal System (EGS) is established on a metal-bearing geological formation, which will be manipulated in a way that the co-production of energy and metals will be possible. The project, at a laboratory scale, intends to prove the concept that the composition and structure of ore bodies have certain characteristics that could be used as an advantage when developing an EGS.

It is also planned to verify that metals can be leached from the ore bodies in high concentrations over a prolonged period of time and this may substantially increase the economics of the EGS. The project also aims to find proof for the concept that continuous leaching of metals will increase the performance of the system over time in a controlled way without having to use high-pressure reservoir stimulation. According to our expectations, this will provide new impetus to geothermal development in Europe. In the frame of the project, a Roadmap will also be developed to support the pilot implementation of CHPM systems before 2025, and full-scale commercial implementation before 2030.

2.2 Scope and structure of Work Package 1

The CHPM2030 project consists of nine work packages. Work package 1 – Methodology framework definition provides a conceptual framework for the technology of energy production and the extraction of metals from ore deposits located at depths below the conventional mining, where the temperature is above 100°C. Within this work package, we synthesise our knowledge of potential ultra deep metallic mineralisations in Europe that could be converted into an "orebody EGS". The characteristics of these bodies and their implications for EGS will also be investigated. By working on the boundaries of geophysics, geochemistry, hydrogeology and geoenergetics we aim to discover and examine the geological, tectonic, geochemical, and petrologic factors that define the boundary conditions of such novel EGS both in terms of energy and potential for metal recovery.

Work package 1 consists of four tasks. Task 1.1 involves literature research and the summarisation of Europe's metallogeny from EGS-relevant aspects. Task 1.2 focuses on the extension of the current metallogenic models to greater depths, based mostly on our knowledge about the test areas, with a complete European outlook. Task 1.3 investigates rock properties at laboratory conditions, and Task 1.4 provides a synthesis of the outcomes of the former tasks within this work package.

2.3 Scope and role of Task 1.3

In the frame of Task 1.3 – Understanding the geochemical and rock mechanical properties of orebodies from an EGS perspective, we have investigated the mineralogical, petrographycal and geochemical features of samples which represent different ore types. The results have been evaluated in a relevancy with the application of the CHPM technology. Methodology for the rock mechanical measurements carried out in Task 2.1, in order to clarify the rock stresses and their impact on fracture formation, is also provided.

3 Methodology

3.1 Role of this deliverable and relation to other work phases

Within Work package 1, there are four deliverables. D1.1 provided a synthesis of our understanding on the types of metallic mineral occurrences that exist at depths below conventional mining. D1.2 summarises the knowledge gaps that need to be filled in order to identify target sites for a future CHPM facility. D1.3 evaluates the CHPM-relevant mineralogical and geochemical characteristics of ore samples. Based on the outcomes from Tasks 1.1–1-3, D1.4 develops overall concept for converting different types of orebodies into an EGS reservoir.

Within the recent deliverable, the geochemistry, mineralogy and texture of different ore types are discussed. It is important, because the methods to be developed in the project will target individual mineral formations taking advantage of their specific geochemical and structural features.

Beside the types of metals which potentially are enriched by the ore-forming processes, it is also substantial to understand the origin and structure of macro- and micro-fracture systems, which are characteristic for the given ore deposit. In order to know more about the formation and nature of the fractures, laboratory tests on rock strength will be carried out in WP2 on the same samples that were used for the mineralogical-geochemical investigations. Both the metal content, the mineralogy, the textural parameters and the rock mechanical features will be taken into consideration during the laboratory experiments on the metal mobilisation (WP2) and the metal recovery (WP3).

3.2 The structure of this document

This deliverable is structured in eight chapters:

In Chapter 1, a short summary of this study is provided.

Chapter 2 is an introductory part. Here, the objectives of the CHPM2030 project are outlined, as well as the structure of Work package 1 and Task 1.3, within which the recent deliverable has been prepared.

In Chapter 3, the aim and the role of the recent document in the implementation of the project are defined and its relation to the other deliverables is described.

Chapter 4 summarises the main characteristics of the ore types which are potential targets of the CHPM technology. These characteristics were described in details in D1.1.

Chapter 5 provides the list and the basic properties of the 26 examined ore and rock samples.

Chapter 6 contains the detailed description of the results from the mineralogical-petrological-geochemical investigations.

In Chapter 7 a CHPM-relevant evaluation of the examinations result is presented.

Chapter 8 describes the methodological framework for the petrophysical and rock mechanical examinations which will be implemented in Task 2.1.

Chapter 9 summarises the conclusions of this study.

Section 10 provides a list of references in which the bibliography used for preparing the recent study is listed.

4   Potential target ore body types and formations identified in D1.1

In the frames of the CHPM project ore is a material from which metallic components of economic value can be extracted, and ore deposit is any permeable rock body from which this extraction is technologically possible via hot aqueous solution. Therefore, the term 'ore body' does not cover the same objects as for the traditional mining.

Ore minerals are not necessarily the ones containing a specific metal in the highest concentration, but the ones most likely decompose or dissolve under physical conditions on the required temperature level of the Earth's crust, releasing the metal to the solvent. On the other hand, the solution has to reach the surface and be processed for the extraction and separation of the metals, simultaneously with extraction of the heat. In a preliminary assessment, the following chemical elements were considered as useful and possible to process: Cu, Zn, Pb, Fe, As, Sb, Cd, Ag, Au, Mn, Co, Cr, Ni, U, Mo. The study was focused on sulphide mineralization carrying these metals. Future tests and gaining experience may modify (broaden or shorten) this list.

The study D1.1 summarized the characteristics of ore deposits of different types, and the distribution of known deposits on the area of the EU member countries. The conclusions identified the most appropriate target types, but also emphasized the fact that almost all knowledge on existing deposits comes from a shallow zone of low temperature. At the start of the project four test areas were chosen with different metallogenetic associations; the characteristics of these areas also were briefly introduced.

Magmatic-hydrothermal mineralization associated with intrusive bodies was the most obvious choice as a genetic process producing potential targets. Mechanical properties of plutonic (mainly granitic) rocks can be considered as appropriate for drilling and maintaining a crack system allowing fluid transport: deep geothermal projects so far were based on such bodies mostly. Syn- and postmagmatic hydrothermal activity can produce mineralization in and around the intrusive bodies. Greisens and veins are typical in the top region, and therefore (unless deeply buried and heated) not as prospective as lower levels of porphyry and skarn mineralization. These lower level mineralization types, however, are hosted mainly by the contact aureole of the intrusion and not by the plutonic rock itself. Most base and precious metals tend to enrich associated with mafic intrusions, whereas granite (or granodiorite) contact zones can host porphyry Cu and Mo, or Sn and W enrichments too. Skarns develop by metasomatism of a carbonate country rock. Typical ore minerals are sulphides and oxides, but a considerable amount of metals can be incorporated by specific silicates and other minerals which can prove unstable under conditions of leaching. Skarn and porphyry mineralization may occur linked in the same magmatic complex, depending on the host rock type and zoning of the metasomatism.

Another metallogenetic environment of considerable potential is a subsiding basin in a rift or subduction zone, where mineralized horizons form as a consequence of submarine volcanism and exhalation. Such ore bodies may be relatively thin, but with large lateral extension. Most important deposit types are the volcanic massive sulphide (VMS) ores, the sediment-hosted (stratiform or stratabound) base metal deposits and the black shale horizons, where metal enrichments are bound to organic matter. The extensional basin setting ensures deep burial and elevated heat flow. As black shale also has a hydrocarbon generating potential, successions containing such beds are often explored already with geophysical means and hydrocarbon wells.

A third possibility lies in the deep-rooted fault zones, mainly those of extensional nature and elevated heat flow. Shallow level hydrothermal ore deposits in this environment often originate from remobilisation of

metals of an earlier mineralization. Occurrence of these deposits may indicate the presence of a deep seated fertile rock body, which can have a potential for further leaching.

Most known deposits of three of the four test areas belong to the intrusion related mineralization types. The Cornubian Ore Field (England) consists of fracture-controlled lodes and veins hosted by a series of batholiths and their metasomatised country rocks. The Banatitic Magmatic and Metallogenic Belt (Romania) and the three mining districts of Sweden (Bergslagen, Skellefte and Northern Norrbotten) expose several skarn and skarn-related deposits, but stratabound and stratiform base metal ores of volcanic origin also occur on these areas. On the fourth area, the Iberian Pyrite Belt (Portugal) these latter ore type is predominant. In all of these regions, deep continuation of the ore bearing complexes is expected. The geothermal gradient and the heat flow are higher than the average in the Cornubian Ore Field, Banatitic Magmatic and Metallogenic Belt and Iberian Pyrite Belt, but not in Sweden.

5   Listing and basic properties of the examined rock samples

The concept of the material testing was to obtain samples representing the test areas and the potential target ore types, and to study the mineralogical and chemical composition, the textural and structural properties and the mechanical strength of these materials. As a first approach, samples were provided by the project partners related to these areas by country. The sample set was then extended by the University of Miskolc because of two reasons:

1. Skarn samples were overrepresented in the set, so pieces of other ore types were chosen from the collection of the university taken from significant, well-explored deposits of the North Hungarian Range.

2. Petrophysical tests, which will be carried out on the same samples in the frame of WP2, Task 2.1, required a minimal diameter which was not met by most of the specimens sent to us, so additional sampling was made on the dumps of an available deposit of the Banatitic Magmatic and Metallogenic Belt.

26 samples of the total collection were used for testing. All samples except sample 22 were cut, and a part of the cut material was pulverised for XRD and XRF measurements. Polished surfaces for ore microscopy and electron microprobe analysis were made on samples containing opaque mineral grains (sulphide and oxide ore minerals). Rectangular sections were positioned on concentrated occurrence of the ore minerals or on boundaries of textural zones if samples were not homogeneous. Thin sections were made from samples of the country rocks and from samples comprising mostly other than opaque minerals.

Mineralogical analyses were qualitative only as samples are not representative for the ore grade of the deposits, but recorded XRD data are appropriate for quantitative analysis if necessary. 9 pieces of rock were chosen as large enough to form the cylinder-shaped body for petrophysical testing performed and reported in WP2. Sample 22 served only as a large sized substitute for sample 12 in these tests, collected at the same site.

The basic data of the samples are summarized in Table 5.1. The mass is given below 3 kg only, indicating scarcity of the material for any further tests. Most samples come from mines, except samples 23–25 which are drillcores from the Iberian Pyrite Belt.

Id	Region	Site	Ore type	Provided by	Mass (kg)	Microscopy	Petrophysics
1	BMMB	Baita Bihor	Skarn	IGR	0.18	r, t	
2	BMMB	Pietroasa	Skarn	IGR	0.98	r, t	
3	HU	Gyöngyösoroszi	Vein	UNIM	1.7	r, t, e	
4	HU	Rudabánya	MVT	UNIM	>3	r, t, e	x
5	HU	Recsk	Porphyry	UNIM	>3	r	x
6	HU	Recsk	Skarn	UNIM	>3	r, e	x
7	COF	Craddock Moor	Porphyry	BGS	>3	r, t	x
8	COF	Herod's Foot	Vein	BGS	2.6	r, t	
9	BL	Dannemora	Country rock	SGU	1.45	r, e	

Id	Region	Site	Ore type	Provided by	Mass (kg)	Microscopy	Petrophysics
10	BL	Dannemora	Skarn	SGU	2.38	r	
11	BL	Dannemora	Country rock	SGU	1.44	t	x
12	BMMB	Cacova Ierii	Skarn	UNIM	>3	r, t, e	
13	BMMB	Cacova Ierii	Skarn	UNIM	>3	r, t, e	x
14	BMMB	Baisoara	Skarn	UNIM	>3	r, t	x
15	BMMB	Budureasa	Skarn	IGR	2.33	r	
16	BMMB	Pietroasa	Skarn	IGR	0.83	r, t	
17	BMMB	Baita Rosie	Skarn	IGR	2.7	r, t, e	
18	BMMB	Pietroasa	Skarn	IGR	1.54	r, t, e	x
19	NNB	Malmberget	Skarn	SGU	2.15	r	
20	SK	Kristinebergsgruvan	Porphyry	SGU	1.46	r, t, e	
21	SK	Kristinebergsgruvan	Porphyry	SGU	1.79	r, t	
22	BMMB	Cacova Ierii	Skarn	UNIM	>3		x
23	IPB	Porto de Mel	Country rock	LNEG	0.41	t	
24	IPB	Porto de Mel	Country rock	LNEG	0.44	t	
25	IPB	Porto de Mel	Country rock	LNEG	0.8	t	
26	IPB	Corvo inferior	VMS	LNEG	2.64	r, e	

Table 5.1 Basic data of the tested samples

Regions: BL – Bergslagen, BMMB – Banatitic Magmatic and Metallogenic Belt (Apuseni Mts), COF – Cornubian Ore Field, HU – Hungary (North Hungarian Range), IPB – Iberian Pyrite Belt, NNB – Northern Norrbotten, SK – Skellefte. *Microscopy:* r – reflected light, t – transmitted light, e – electron microprobe.

The *macroscopic characteristics* of the samples are shortly described below; photographs of the samples are shown in Figures 5.1–5.5:

Sample 1   Molybdenite ore with disseminated molybdenite grains within a cream coloured matrix.

Sample 2   Represents a borate mineralization with hardly any opaque minerals and abundant calcite where whitish material contains dark acicular minerals enriched in nests.

Sample 3   A fragment of a calcite vein with base metal sulphides.

Sample 4   Banded baritic lead ore from a metasomatic deposit hosted by limestone; galena grains in dark bands can be recognized with coarse grained white barite lenses and fine grained limonitic matrix.

Sample 5   Represents an intrusion related porphyry copper deposit; a breccia with sulphide matrix and veins.

Sample 6	Originates from the same site as Sample 5. It is a massive pyrite-chalcopyrite-iron oxide ore from the skarn zone.
Sample 7	It represents brecciated quartz hosted chalcopyrite, a hydrothermally formed porphyry ore from a granitic intrusion.
Sample 8	Structure-bound galena ore in a foliated dark metasedimentary rock.
Samples 9	Skarn type magnetite deposit, contains lens-shaped, dark inclusion with greenish (epidote enriched) rims.
Sample 10	Skarn type magnetite deposit, massive ore.
Sample 11	Skarn type magnetite deposit, host carbonate.
Sample 12	Represents a magnetite deposit also enriched in sulphides, with visible chalcopyrite.
Sample 13	Represents a magnetite deposit also enriched in sulphides, with visible chalcopyrite.
Sample 14	Represents a magnetite deposit also enriched in sulphides, with visible chalcopyrite.
Sample 15	Magnetite ore with no visible sulphides.
Sample 16	From a borate mineralization, with magnetite enrichment within calcite.
Sample 17	Diopside dominated skarn with some magnetite and molybdenite.
Sample 18	Originates from a borate mineralization with hardly any opaque minerals and abundant calcite where whitish material contains dark acicular minerals enriched in nests.
Sample 19	Magnetite ore with no visible sulphides.
Sample 20	Chalcopyrite containing sulphide ores in a hydrothermally formed, coarse grained quartz-dominated host rock related to a major VMS deposit.
Sample 21	Chalcopyrite containing sulphide ores in a hydrothermally formed, coarse grained quartz-dominated host rock related to a major VMS deposit.
Sample 22	Represents a magnetite deposit also enriched in sulphides, with visible chalcopyrite.
Sample 23	Fine-grained, brecciated volcanic rock with white veins.
Sample 24	Fine-grained volcanic rock with white veins.
Sample 25	Fine-grained volcanic rock with white veins, contains disseminated sulphide grains.
Sample 26	Banded volcanic massive sulphide ore dominated by pyrite and chalcopyrite, also containing sphalerite and cassiterite in undulated, anastomosing bands of variable thickness.

Figure 5.1 Photographs after cutting, but before processing of Samples 1–6 (from upper left to lower right).
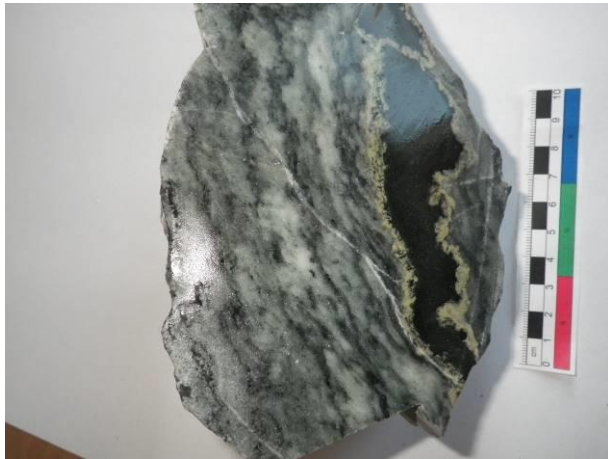
Figure 5.2 Photographs after cutting, but before processing of samples 7–12 (from upper left to lower right).
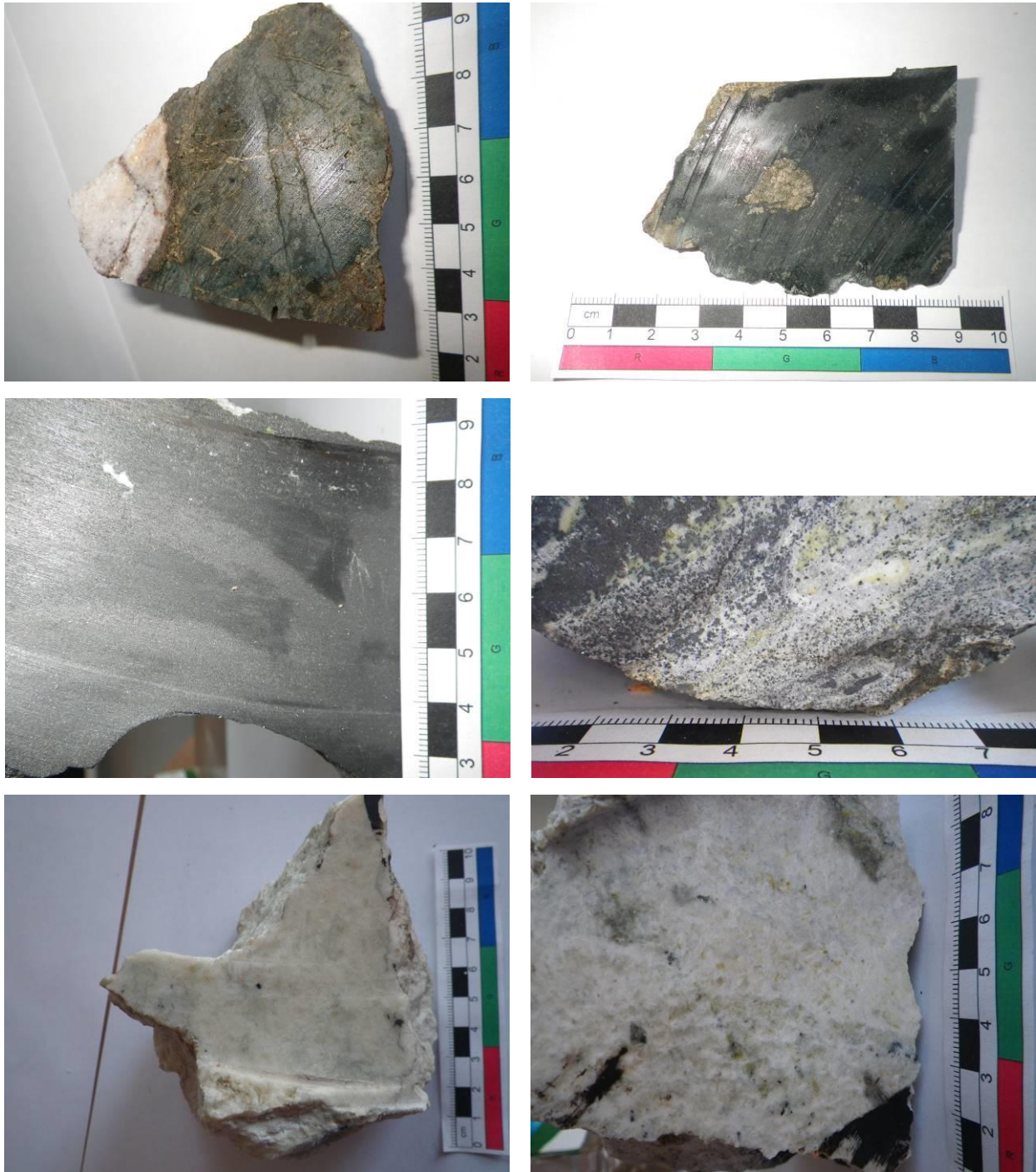
Figure 5.3 Photographs after cutting, but before processing of samples 13–18 (from upper left to lower right).

Figure 5.4 Photographs before processing of samples 19–21 (from left to right).
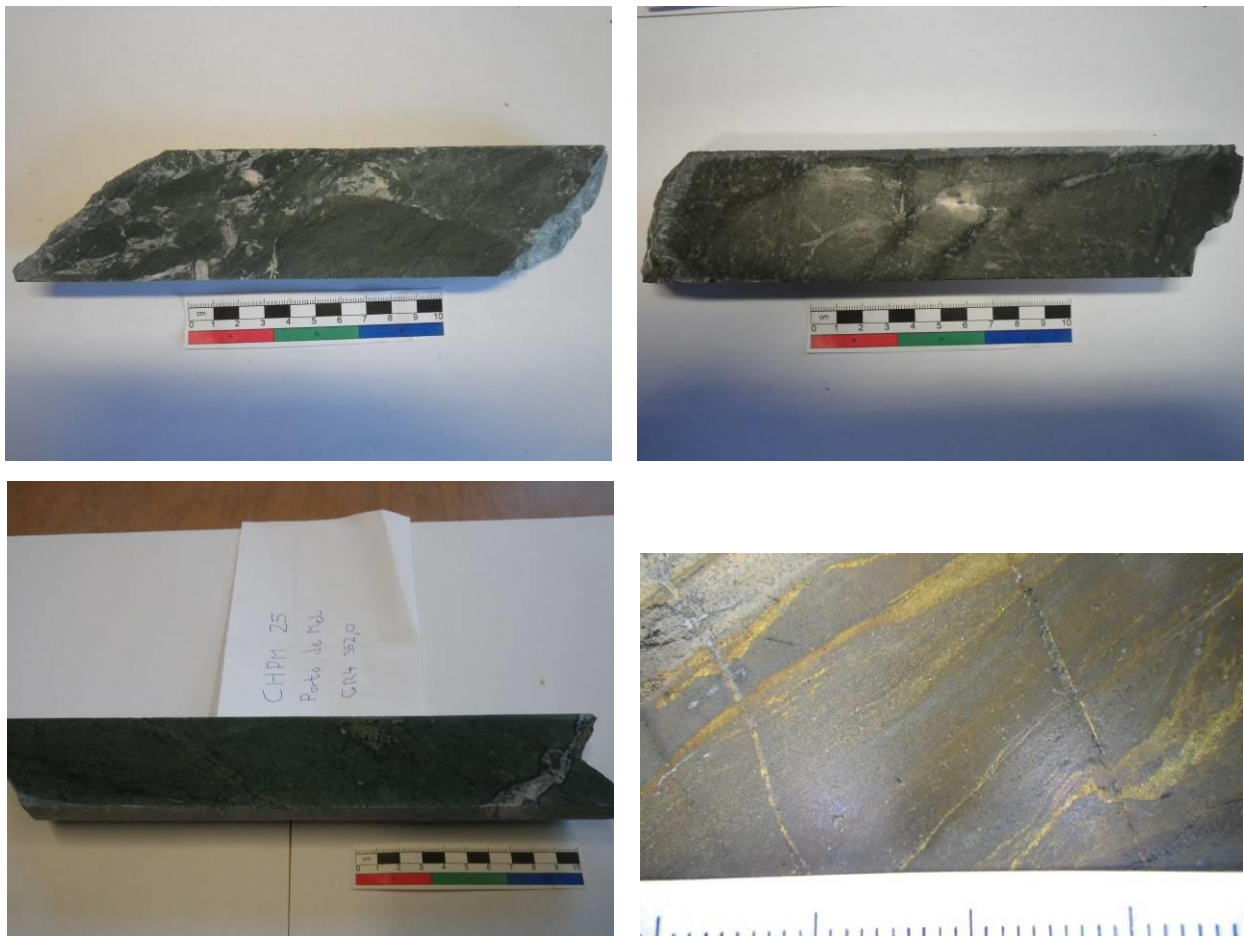
Figure 5.5 Photographs before processing of samples 23–26. Cut surfaces were given on the samples sent to the UNIM (from upper left to lower right).

6   Mineralogical and geochemical studies

6.1   X-ray diffraction investigations

Samples were prepared by hand-grinding in porcelain and agate mortars. Specimens were prepared in top-loaded sample holders (~ 1 g). Investigations were carried out on a Bruker D8 Advance diffractometer (Cu-Kα radiation, 40 kV and 40 mA generator settings), with vertical goniometer, in parallel beam geometry obtained with Göbel mirror and Vantec1 position sensitive detector (1° window opening). Measurements were taken in the 2–70° (2θ) angular region, with 0.007° (2θ)/29 sec recording.

Identification of crystalline components was done with Search/Match algorithm in Bruker DiffracPlus EVA, after Fourier noise reduction and polynomial background subtraction of raw patterns. The Powder Diffraction Files (PDF) database of International Centre for Diffraction Data (ICDD) was used.

The following mineral phases were identified in the samples:

Sample 1	The main component is grossular, with possible Fe-substitution, accompanied by diopside, molybdenite and quartz. Minor wollastonite and calcite content is also detected.
Sample 2	The main component is calcite and Mg-bearing calcite, as indicated by peak maximum values. Alongside with clinochlore (Mg-rich), several minor minerals were identified as possible components: borates of szaibelyite > ludwigite comnposition, sjogrenite (?), doyleite (?) and traces of kaolinite. Several minor peaks remain unsolved, possibly belonging to mixed species of borate end-members.
Sample 3	The main component is Mg-bearing calcite, with minor quartz, sphalerite and galena. Traces of pyrite and kutnohorite were also detected.
Sample 4	The main component is galena with barite and cerrusite, with important smithsonite, quartz and bindheimite. Minor bernalite and goethite with trace amounts of muscovite and dolomite were also detected.
Sample 5	The main component is quartz, with major magnetite and pyrite, possibly maghemite content. The maghemite-like structure might also be a result of Fe-substitution in magnetite.
Sample 6	The main components are chalcopyrite and pyrite with major actinolite content. Minor presence of magnetite, quartz and diopside is observed, with traces of andradite.
Sample 7	The main component is quartz, with pyrite and minor amounts of schörl.
Sample 8	The main component is quartz, with major galena content. Minor presence of dolomite, illite and tennanite is detected, with trace amounts of pyrite and clinochlore.
Sample 9	The main component is calcite with Mg-bearing calcite, accompanied by minor quartz, epidote and orthoclase. Biotite is also detected, with strong preferred orientation. Presence of zeophyllite is not reliable by XRD alone.
Sample 10	The main component is magnetite, with small amount of antigorite (possibly other serpentine species) and minor amounts of actinolite, pyrope and spessartine. The peak tails of magnetite indicate substitutions of Fe in its structure, possibly by Zn (franklinite components) and Mg (magnesioferrite component).

Sample 11	The main component is quartz and calcite. Important amounts of microcline, epidote and albite are observed. Biotite is present in trace amounts. A high Mg-bearing calcite presence is also possible.
Sample 12	The main components are pyrite, magnetite and dolomite, with important amounts of galena. Magnetite might have Zn or Ti substitution as indicated by low-angle peak tails. Some minor peaks remain unresolved.
Sample 13	The main component is "hydrogarnet" type material, hibshite-katoite mixture and grossular (possibly Fe-bearing). Major pyrite and diopside, minor quartz and calcite are detected.
Sample 14	The main component is actinolite, with important quartz and pyrite content, and minor low Mg-bearing calcite.
Sample 15	The sample is made up by magnesioferrite, with traces of magnesite.
Sample 16	The main component is ankerite > dolomite double carbonate phase, with important fluorite, magnetite and antigorite +/- lizardite. Minor amount of Mg-bearing calcite is also detected.
Sample 17	The main component is diopside, with major calcite content. Minor presence of talc, lizardite, quartz and traces of fluorite are detected also. Diopside is possibly Fe-bearing, less likely Co bearing, but the crystal structure resulting from atomic substitution are similar.
Sample 18	The main component is calcite, with important szaibelyite content. Minor amounts of clinochlore and lizardite are detected also.
Sample 19	The sample is constituted by magnetite with traces of actinolite.
Sample 20	The main components are quartz and Fe-rich clinochlore, with major pyrite and chalcopyrite content. Possibility of serpentine traces presence exists.
Sample 21	The sample is made up by quartz, with important pyrite and trace contents of chalcopyrite.
Sample 23	The main component is quartz, Mg-bearing calcite and albite (possibly oligoclase-andesine components). Important contribution of Fe-rich clinochlore and muscovite is also observed.
Sample 24	The main component is quartz and albite (possibly oligoclase-andesine components). Minor contribution of Mg-bearing calcite, Fe-rich clinochlore and muscovite is observed. Pyrite is detected in trace amounts.
Sample 25	The main component is quartz and albite (possibly oligoclase-andesine components). Important contribution of Mg-bearing calcite, Fe-rich clinochlore and muscovite is observed.
Sample 26	The main component is chalcopyrite, with major pyrite and sphalerite. Minor contribution of cassiterite is detected, with traces of siderite.

6.2 X-ray fluorescence spectrometry

X-ray fluorescence spectrometry (XRF) is a universal method for the determination of the chemical composition of the sample, by using the detection of interaction between X-ray and elements in the analysed sample. If the energy is detected, it is defined as energy dispersive system (EDX), if the wavelength is measured, it is a wavelength dispersive system (WDX). The EDX system detects all the element from [9]F to [92]U in the same time, but the detection limit is around 0.5-1% or even higher. The WDX system measures simultaneously only one element, but the detection limit is 3 or 4 magnitudes lower. It is in ppm or 10 ppm range.

In sample preparation, the grain size of the sample was crushed under 65 μm in a ceramic mortar, then it was dried out on 120°C at 2h. The decreasing of mass was measured and loss of moisture (LOM) was calculated (see Table 6.3.). From the already dried powder 4.000 g was measured out and mixed by Cereox binder in 4 to 1 ratio and homogenized in an agate mortar. This mixture was pressed into diameter of 32mm pellet by pressure of 25 tones. Determination of loss of ignition (LOI) was done on 1050°C with 10°C/min heating up and 15min heat kept at 1050°C. The results (see in Table X.3.) are various as the samples contain ignitable components in different ratio.

On the pellets, the analyses both for main and trace elements were completed by a Supermini 200 type WDXRF from Rigaku, which has an air cooled 200 W X-ray tube with Pd target. The radiation is induced by 50 kV and 4.00 mA. Both the calibration and measuring of each element was done at 1.2-1.6 Pa pressure with ZSX driver and evaluation programme. Both in case of main and trace elements, the peak angle positions of the elements were measured for 40 s, while the two background angles were measured for 10 s on LiF200, PET and XR25 crystals. To statistically minimalism the mistakes from measuring, each element was measured 15 times. The main properties of the calibration for main elements are listed in Table 6.1., and for trace elements in Table 6.2. In case of Cu, Zn, Pb and As elements the parameters of accuracy and the correction cannot be defined, because for these elements one-point calibration was done on higher concentration standards.

Element	SiO_2	Al_2O_3	MgO	CaO	Na_2O	K_2O	Fe_2O_3	MnO	TiO_2	P_2O_5	S	F
Det. lim.	0.1	0.1	0.01	0.01	0.01	0.01	0.01	0.005	0.005	0.005	0.005	0.25
Acc.	0.76	0.65	0.14	0.11	0.14	0.18	0.28	0.009	0.033	0.019	0.005	0.10
Corr. fac.	0.997	0.958	1.000	1.000	0.994	0.993	0.994	0.995	0.992	0.980	1.000	1.000

Table 6.1 Properties of calibration for main elements
Det. lim.: detection limit (%); Acc: Accuracy, based on calibration points fitting on calibration curve (%); Corr. fac.: Correction factor.

Element	Cu	Zn	Pb	Rb	Sr	Ba	As	Cr	Co	Ni	Zr
Det. lim.	10	10	10	10	10	25	10	10	10	10	10
Acc.	-	-	-	23	11	10	-	8.8	2.5	5.2	4.0
Corr. fac.	-	-	-	0.986	0.998	0.999	-	0.969	0.977	0.991	0.999

Table 6.2 Properties of calibration for trace elements
Det. lim.: detection limit (ppm); Acc: Accuracy, based on calibration points fitting on calibration curve (ppm); Corr. fac.: Correction factor.

Sample ID	LOM	SiO$_2$	Al$_2$O$_3$	MgO	CaO	Na$_2$O	K$_2$O	Fe$_2$O$_3$	MnO	TiO$_2$	P$_2$O$_5$	S	F	LOI
	%	%	%	%	%	%	%	%	%	%	%	%	%	%
1	0.23	39.7	7.5	2.48	19.7	0.05	0.28	5.21	0.445	0.039	0.218	7.6	<0.25	5.8
2	0.41	7.7	2.4	22.1	33.2	<0.01	0.01	1.48	0.105	0.111	0.049	<0.005	<0.25	28.8
3	0.22	3.7	0.3	0.37	49.8	<0.01	0.03	1.31	0.666	<0.005	0.049	1.8	<0.25	38.5
4	0.15	3.1	0.3	0.1	1.1	1.2	1.4	1.2	<0.005	<0.005	<0.005	13.2	<0.25	3.7
5	0.36	59.6	1.6	0.47	0.49	0.04	<0.01	36.5	0.073	0.481	0.009	11.0	<0.25	4.8
6	0.39	15.8	1.2	4.5	8.8	0.8	1.1	32.9	0.11	<0.005	0.072	29.6	<0.25	13.7
7	0.16	75.1	3.9	0.20	0.09	0.2	0.06	13.4	0.015	0.239	0.072	14.3	<0.25	9.5
8	0.25	69.7	8.2	2.0	7.8	1.8	4.6	3.6	0.24	0.52	0.038	1.8	<0.25	4.3
9	0.14	13.7	3.1	0.51	40.4	0.01	2.34	2.15	0.251	0.052	0.051	<0.005	<0.25	29.9
10	0.21	18.0	0.5	6.67	2.48	<0.01	<0.01	64.7	7.0	0.008	<0.005	0.032	<0.25	0.5
11	0.15	44.7	8.3	1.23	21.0	0.65	3.61	2.53	0.214	0.091	0.044	<0.005	<0.25	2.2
12	0.61	2.6	0.4	6.19	8.54	<0.01	<0.01	39.8	0.070	<0.005	0.011	31.2	<0.25	18.7
13	0.83	32.8	4.2	3.42	21.4	0.05	<0.01	15.9	0.220	0.170	0.097	13.1	<0.25	4.8
14	1.29	46.9	0.5	4.81	11.20	0.08	<0.01	28.2	0.569	0.010	0.077	3.8	<0.25	4.1
15	0.15	2.6	0.5	6.48	0.61	0.03	<0.01	84.6	1.46	0.016	0.037	<0.005	<0.25	0.7
16	0.44	13.3	0.1	19.5	23.8	0.01	<0.01	15.8	0.847	0.007	0.023	<0.005	5.3	21.0
17	1.24	47.3	0.1	21.5	19.2	0.02	0.04	0.44	0.270	<0.005	0.020	0.01	1.2	9.9
18	0.26	1.7	0.5	26.4	34.7	<0.01	0.02	0.33	0.169	0.021	0.036	<0.005	<0.25	35.1
19	0.03	2.6	0.4	1.44	0.55	0.06	<0.01	90.9	0.043	0.841	0.097	<0.005	<0.25	0.3
20	0.42	33.6	8.2	5.90	0.03	0.04	<0.01	24.5	0.136	0.087	0.013	19.9	<0.25	15.2
21	0.12	74.9	1.9	0.08	0.03	0.15	0.14	14.2	<0.005	<0.005	0.010	18.3	<0.25	10.8
23	0.38	46.9	11.8	4.00	13.7	1.46	1.94	3.67	0.471	0.413	0.093	<0.005	<0.25	14.6
24	0.44	56.5	13.1	4.57	5.07	1.74	1.74	5.89	0.214	0.559	0.094	0.032	<0.25	9.5
25	0.34	53.8	15.3	3.19	6.06	2.44	2.31	5.10	0.166	0.606	0.105	<0.005	<0.25	9.2
26	0.07	0.7	0.4	0.06	0.10	0.6	<0.01	43.4	0.006	<0.005	0.010	40.2	<0.25	19.0

Table 6.3 Main element composition of the samples with loss of moisture and ignition results.

Sample ID	Cu	Zn	Pb	Rb	Sr	Ba	As	Cr	Co	Ni	Zr
	ppm	ppm	ppm	ppm	ppm	ppm	ppm	ppm	ppm	ppm	ppm
1	24	<10	12	<10	<10	40	<10	29	<10	14	<10
2	10	266	405	<10	54	<25	434	29	<10	<10	23
3	54	0.52%	575	<10	174	<25	90	16	<10	<10	19
4	110	3.8%	7.2%	<10	0.59%	19.1%	0.27%	180	<10	<10	59
5	0.53%	92	20	<10	<10	<25	<10	58	<10	10	<10
6	14.5%	890	190	<10	130	460	<10	230	120	940	<10
7	0.17%	113	0.26%	<10	15	101	0.28%	45	66	<10	53
8	460	240	4.5%	<10	<10	<25	<10	440	<10	<10	<10
9	<10	27	<10	40	41	0.27%	<10	18	<10	<10	38
10	23	22	24	<10	<10	94	10	41	<10	<10	<10
11	<10	29	23	70	49	0.23%	<10	30	<10	<10	97
12	693	<10	13	<10	<10	<25	<10	34	<10	<10	<10
13	400	54	31	<10	<10	<25	14	52	<10	<10	17
14	276	75	<10	<10	10	<25	<10	38	<10	28	<10
15	<10	170	<10	<10	<10	<25	<10	54	<10	<10	<10
16	<10	143	42	<10	29	<25	26	26	<10	<10	<10
17	689	178	679	<10	<10	<25	89	44	18	<10	<10
18	<10	144	118	<10	59	<25	118	21	<10	<10	11
19	<10	<10	<10	<10	<10	<25	<10	105	<10	29	<10
20	2.2%	0.17%	50	<10	75	<25	<10	105	<10	<10	32
21	3.5%	1.0%	170	<10	<10	<25	<10	240	160	<10	<10
23	56	49	<10	24	345	35	<10	48	11	20	126
24	35	77	50	40	114	189	39	61	23	41	119
25	<10	74	12	37	366	144	<10	60	12	38	162
26	23.5%	15.8%	0.16%	<10	<10	45	184	31	358	<10	<10

Table 6.4 Trace element composition of the samples (in the concentration is below 1000 ppm, unit of ppm, if it is beyond1000 ppm, unit of % is used).

By the calibration of each element, the prepared pellets from the samples were measured. In case of sample CHPM 4 and 6 1:9; CHPM 8 1:19 and CHPM 26-27 1:49 dilution was necessary to be done to dilute the trace elements into the well measurable concentration range. This also helped to avoid the strong matrix effect of the heavy metals for each other and also for the other elements. The dilution resulted that less decimals are given in the results, compared to undiluted samples.

To be able to see the non calibrated elements, continuous scan was done on each sample with LiF200 crystal in range from 10° to 90°, to check the presence of the element from [21]Sc to [92]U. Only those samples are listed (Table 6.5.), where at least one element was indicated, which is not in the set of calibrated trace elements (Table 6.4.). Sharp concentration results cannot be defined, but this type of qualitative analysis the concentrations can be split at least into three concentration categories.

Sample ID	^{23}V	^{31}Ga	^{32}Ge	^{34}Se	^{39}Y	^{41}Nb	^{42}Mo	^{47}Ag	^{48}Cd	^{50}Sn	^{51}Sb	^{74}W	^{83}Bi
1	+	+			+		+++			+			
4						+		+	+		+++		
5				+			+						
6				+	+		+						
7		+				+				+			+
8								+		+			
11						+							
12											+		
13										+			
14							+						
16			+										
17													+++
18				+									
19	+												
20		+				+							
21												+	+
23			+										
24			+										
25		+				+							
26										+++	+++		+

Table 6.5 Presence of the non-calibrated elements in range of ^{21}Sc and ^{92}U

Labels: empty cell: below detection limit; +: a few 10 ppm; ++: a few 100 ppm;
+++: concentration in 1000ppm range or over.

6.3 Rock and ore microscopy

25 samples have been examined by means of polished sections for ore mineralogy and/or by thin section for rock forming and gangue minerals. Most samples arrived from different skarn deposits, some of them from hydrothermal and magmatic deposits. One sample arrived from Corvo, representing a massive sulphide deposit type.

Samples were classified where it was possible according to their ore mineral textures. We could differentiate 6 texture groups with 2-5 samples per each. Three samples were not classified; they are kept separate.

6.3.1 Texture group 1: Skarn rocks with very few ore minerals. Ore minerals appear only in small (0.5-1 mm) patches or as alteration / oxidation products after mafic minerals.

Five samples (including host rocks) were classified in this group:

• 2 and 18: borate-bearing skarn,

• 17: diopside skarn,

• 9 and 11: magnetite-bearing skarn.

<u>**Sample 2:**</u> Calcite-borate dominated skarn rock with minor patches and stringers of hematite

Reflected light microscopy: Packages of hematite plates appear along fractures and in small (0.2-0.5 mm) aggregates (fig. 6.1). Sometimes the hematite has been altered to goethite. Relics of opacitized mafic crystals are also found, the opacitized parts turned to hematite as well. Some tiny (0.1 mm), anhedral magnetite crystals appear in the Ca-silicate skarn rock.

Transmitted light microscopy: The most important part of the material is the cryptocrystalline, colourless and transparent groundmass (up to 60 %), with fibrous to lamellar serpentinite nests. Veinlets and nodules of pyroxene (ortho- and clino-) > quartz > intermedier plagioclase are developed, associated with opaque euhedral minerals and low transparency, brown to orange pleochroic crystals (possibly ludwigite). In the groundmass subeuhedral, rounded garnet crystals are observed, with well visible anisotropy related to fissures cross-cutting crystals. This observation is attributed to hydration of garnet and development of "hydrogarnet" species. Calcite with interstitial development is observed in several percents amount. Relicts of coarse grained orthopyroxenes are also found, presumably formed as interstitial phases of a garnet hornfels (Fig 6.2).
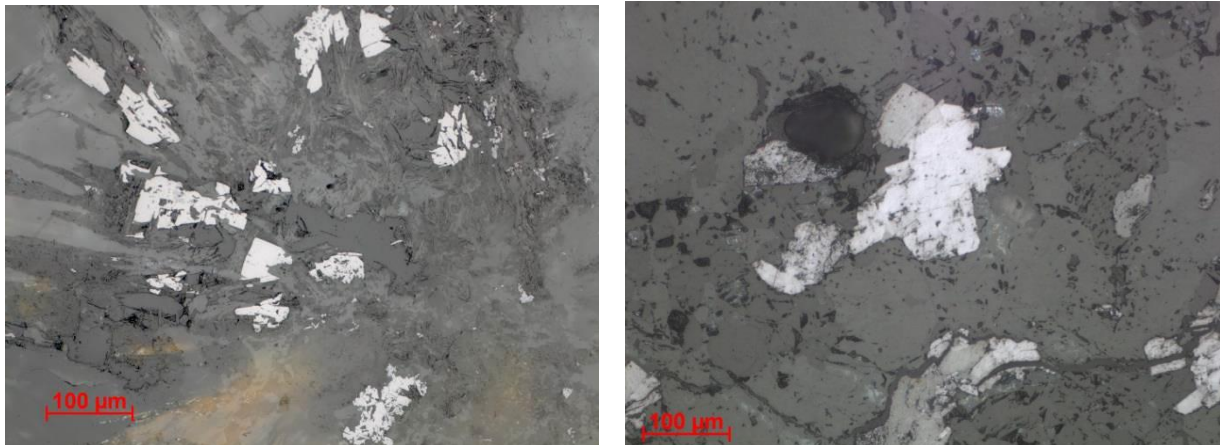
Figure 6.1 Left: Partly opacitized (hematite) mafic mineral grains (white) (RL PPL). Right: Anhedral magnetite and hematite in the matrix (RL PPL).
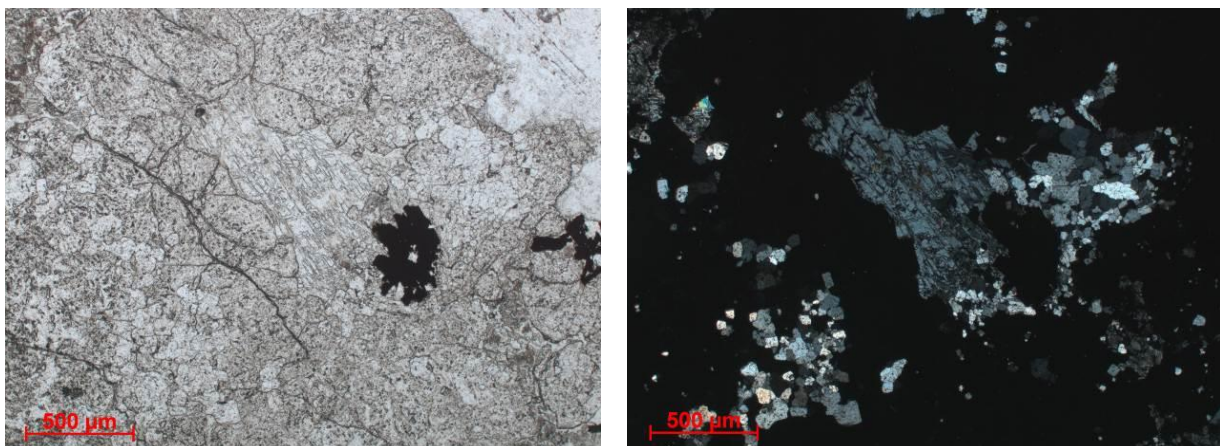
Figure 6.2 Relict orthopyroxene in garnet (isotropic) and calcite (anisotropic) matrix (TL PPL and XPL).

<u>**Sample 18:**</u> Calcite-borate dominated skarn rock with minor patches and stringers of hematite

Reflected light microscopy: Ore minerals were detected only in a few parts as hematite, replacing partially the mafic rock forming minerals.

Transmitted light microscopy: The rock is composed mainly of coarse-grained anhedral calcite crystals. In zones the calcite crystals have many small oval inclusions and acicular crystals (Fig. 6.3). Sheaf-like aggregates with very thin, acicular crystals appear between the calcite grains. Based on XRF and XRD analysis the acicular crystals are szaibelyite or ludwigite. Tiny microcrystalline masses are found around relics of silicate minerals.
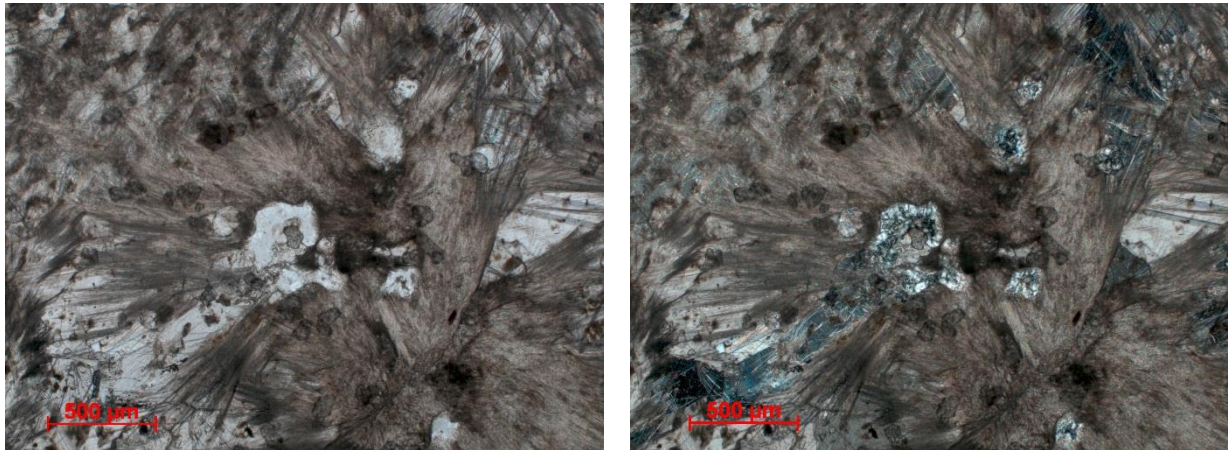
Figure 6.3 Calcite, rounded lizardite and acicular szaibelyite (TL PPL and XPL).

Sample 17: Diopside skarn rock

Reflected light microscopy: Tiny molybdenite(?) patches (<0.1 mm) developed rarely along fissures and embedded in the calcite (Fig. 6.4 right). Mafic minerals altered to magnetite and partly ilmenite and tiny magnetite (< 0.1 mm) embedded along calcite grains. Ore minerals comprise 1-2%.

Transmitted light microscopy: Main mass of the rock is composed of corroded, large (2-5 mm) diopside / augite crystals (75%). Calcite and talc developed along cracks and interstitial zones. Calcite sometimes replaces completely the pyroxene crystals (15%). Talc develops along fissures and in sheaf-shaped aggregates (ca. 8%) (Fig. 6.4 left).
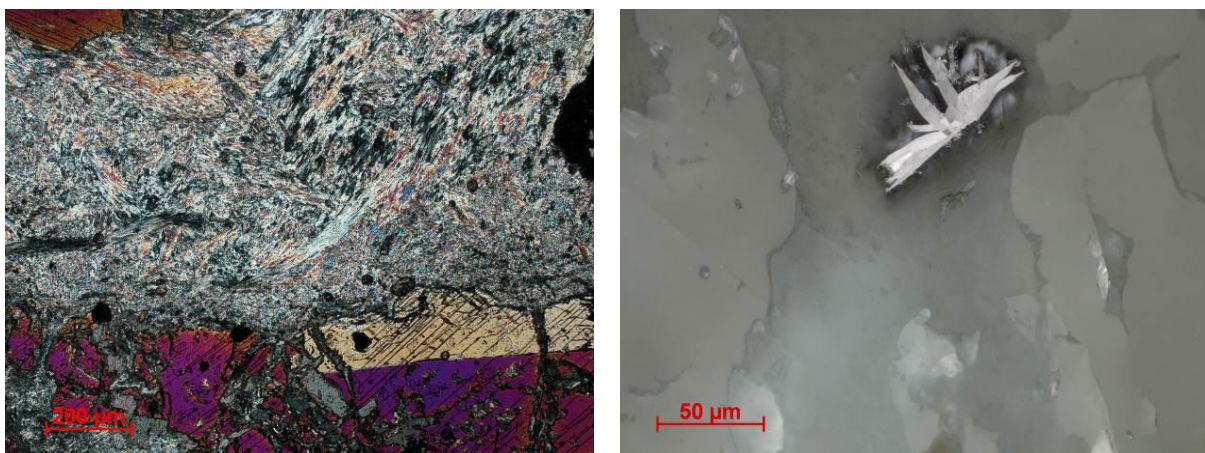
Figure 6.4 Left: Twinned diopside crystals (bottom) fragmented and accompanied by acicular talc (TL XPL). Right: Tiny molybdenite crystals in calcite (RL PPL).

Sample 9: calcite skarn rock

Reflected light microscopy: Not any ore minerals were detected in the sample

Sample 11: calcite skarn rock

Transmitted light microscopy: The sample appears to represent a replacement type alteration, preserving dolomitised or Mg-bearing calcite relicts (up to 50-60 %) in a fine grained calcite groundmass (Fig. 6.5). Linked to these rounded relict masses significant epidote is observed, in very fine grained, altered anhedral grains. This texture and composition is assumed to be the result of a metasomatic alteration of a silicate rock, which also explains the presence of microcrystalline quartz nodules attached to the relicts. Opaque grains are not observed. Epidote-clinozoisite is also found among the transformation products, as micrometric prismatic to lamellar crystals. Accessories of biotite (+/- phlogopite) and chlorite are observed in the fine grained calcite product.
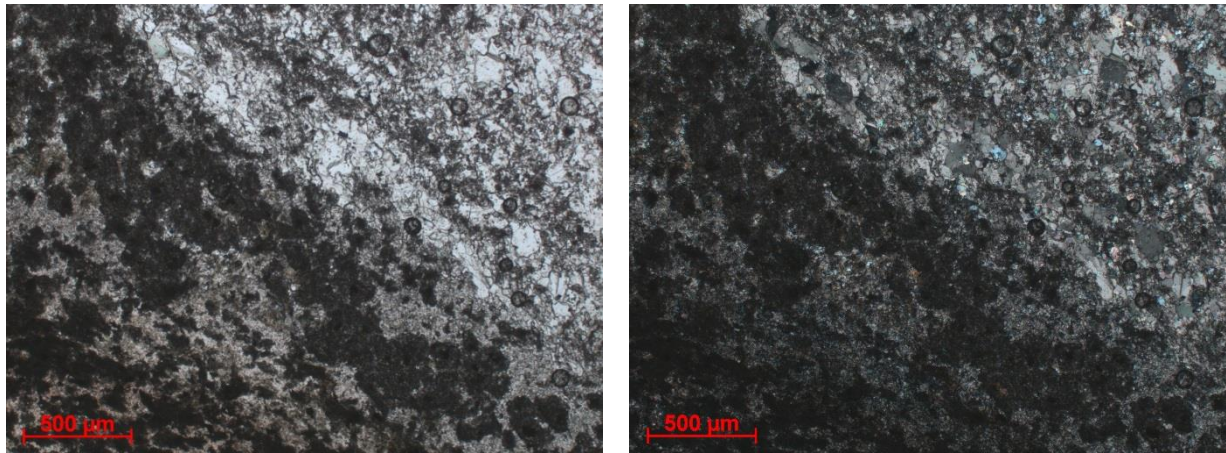
Figure 6.5 Calcite (bright) and epidote (high interference colours) grains in fine grained calcite matrix (TL PPL and XPL).

6.3.2 Texture group 2: Contactised rocks with irregular cracks, filled by ore minerals. Cracks form 0.5-1.5 mm thick fissures.

Two samples were classified in this group:

• 1: skarn molybdenite ore,

• 8: metasomatic galena ore.

Sample 1: Molybdenite ore developed along fissures in calcite-rich skarn

Reflected light microscopy: Packages of molybdenite with size of 0.1-0.3 mm plates form massive fissure fillings with irregular path in the carbonate-rich skarn rock (Fig. 6.6 left). Sometimes molybdenite forms porphyric texture in the rock. Molybdenite is the only ore mineral and comprises 2-3% of the sample.

Transmitted light microscopy: Calcite-rich skarn rock with Ca-silicates. Main rock forming mineral is clacite, appearing in 0.3–1 mm sized, anhedral grains. In one part of the sample, along the calcite grains anhedral hydrogarnet grains appear very often, reaching 0.1 mm (Fig. 6.6 right). In this part, the calcite grains contain wollastonite needles reaching 0.2–0.3 mm length. Along 0.2–0.5 mm thick zones the wollastonite forms massive, oriented aggregates. In the other part of the sample, wollastonite is found along the calcite grains more often compared to hydrogarnet.
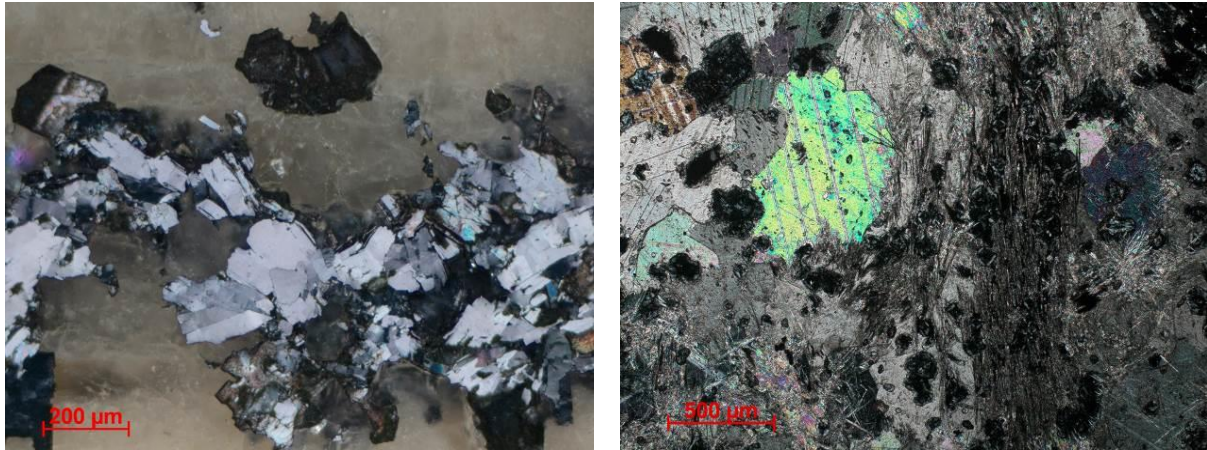
Figure 6.6 Left: Molybdenite crystals (variegated grey) developed along an irregular fissure (RL XPL). Right: Anhedral calcite crystals bordered by hydrogarnet grains (nearly black spots) and acicular crystals of wollastonite (dark grey) (TL XPL).

Sample 8: Brecciated shale with galena in fissures

Reflected light microscopy: Galena as the principal ore mineral appears in anhedral grains, filling irregular cracks. Galena masses in some parts reach 3-5 mm thickness. Galena grains are slightly oxidized along their borders. Rarely chalcopyrite and pyrite appears at the rim zone of the galena or as inclusions in it, reaching 0.1 mm (Fig. 6.7 right).

Bacterial pyrite can rarely found in small aggregates in the shale.

Transmitted light microscopy: The rock is composed of clay minerals, having strongly oriented texture. This shale is fractured along the schistosity plane and at adjoined fissures filled by microclystalline quartz. Widely opened fissures are filled by quartz crystals of 0.1–0.3 mm size (Fig. 6.7 left), dolomite/ankerite crystals reaching 0.5 mm and by the galena ore.
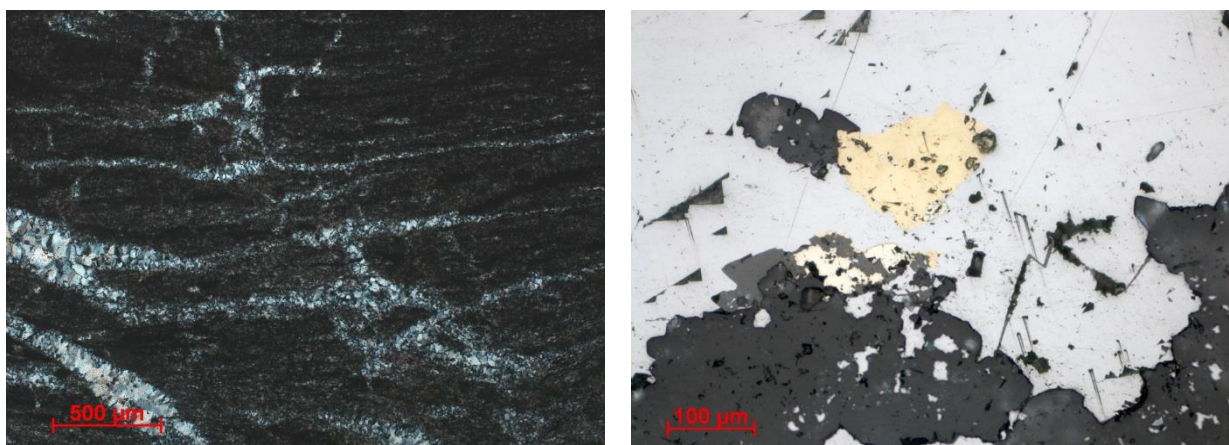
Figure 6.7 Left: Fractured shale, fissures are filled with microcrystalline quartz (TL XPL). Right: Galena grain (white) with inclusions of pyrite (creamy) and chalcopyrite (yellow) (RL PPL).

6.3.3   Texture group 3: Massive magnetite ore, having cracks and micro-fissures

Three samples were classified in this group:

•   10: massive magnetite ore sample

•   15: massive magnesioferrite ore sample

- 19: massive magnetite ore sample

Sample 10: Massive magnetite ore

Reflected light microscopy: Massive ore, mineral grains cannot be distinguished. Massive magnetite is cut by microcracks with several mm length, filled by gangue minerals (Fig. 6.8 left). The massive ore includes 0.1–0.3 mm sized relics of silicates, forming poikilitic texture. At the edge of the massive ore, connected to a 1 mm thick veinlet filled by fine-grained quartz, pyrrhotite occurs interlocked with magnetite (Fig. 6.8 right). Some tiny (0.05 mm) pyrite and very rarely chalcopyrite appears in the veinlet embedded by quartz.

Transmitted light microscopy: Massive ore, thin section was not made
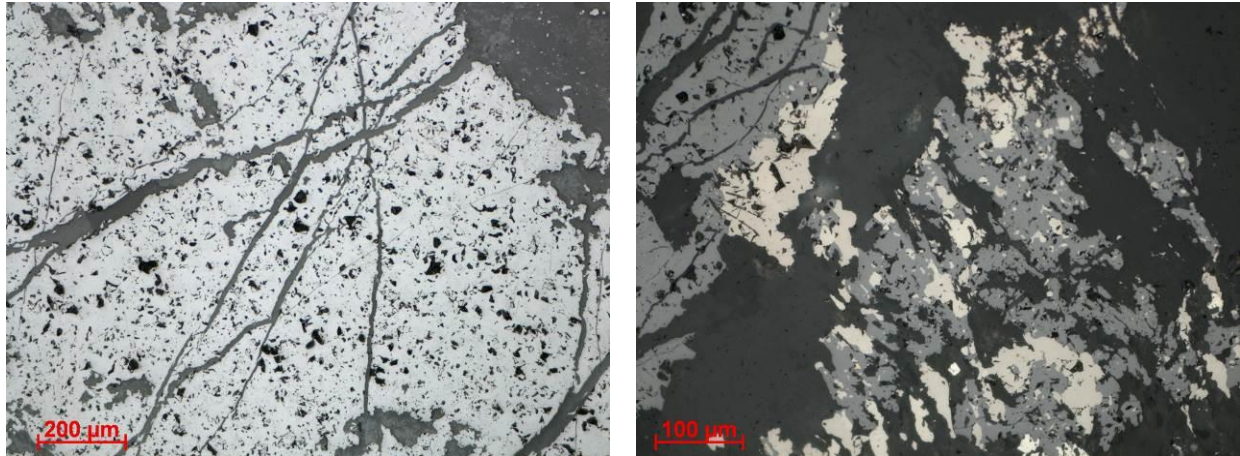
Figure 6.8 Left: massive magnetite (white) with fissures (RL PPL). Right: Pyrrhotite (creamy) intergrown with magnetite (grey) (RL PPL).

Sample 15: Massive magnetite ore

Reflected light microscopy: Massive, homogeneous magnesioferrite sample. Anhedral magnesite crystals occupy voids and veins similarly like on Fig. 6.8 (left) in sample 10.

Sample 19: Massive magnetite ore
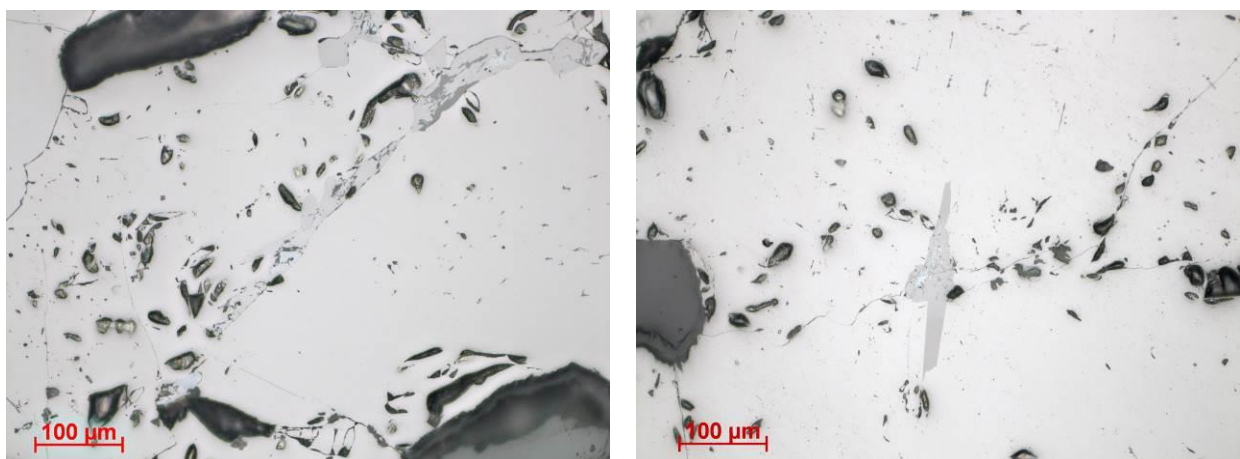
Figure 6.9 Left: Massive magnetite (white), hematite (lighter) and ilmenite (darker) occur as fissure filling (RL PPL). Right: Massive magnetite grain (white) with ilmenite (grey) developed at a fissure (RL PPL).

Reflected light microscopy: Massive magnetite sample, composed of isometric magnetite crystals with 0.2–0.7 mm size. The texture is polygonal, magnetite crystals interlock 120° angles at triple borders. Along micro-

fissures the magnetite is altered to hematite and ilmenite (Fig. 6.9). The latter minerals comprise 2-5% of the sample.

Transmitted light microscopy: Massive ore, thin section was not made

6.3.4   Texture group 4: Pyrite-rich porphyric ore with considerable amount of chalcopyrite

Four samples were classified in this group:

*   5: metasomatic porphyry Cu ore

*   6: metasomatic massive Cu ore

*   7: metasomatic porphyry Cu ore

*   20: metasomatic porphyry Cu ore

<u>Sample 5:</u> Porphyric pyrite-magnetite-chalcopyrite ore

Reflected light microscopy: 60% of the sample is composed of ore minerals with a quite complex texture. Ore minerals comprise the matrix of the sample, embedding quartz-rich inclusions with 10–15 mm diameter. Composition of the matrix changes from pyrite-dominant parts to magnetite and/or chalcopyrite rich parts.

The 15 mm thick quartz grain that is found in the central part of the sample is fractured to 1–2 mm subgrains. Along the micro-cracks, the quartz holds anhedral inclusions of pyrite and chalcopyrite. Size of the inclusions varies between 0.05–0.4 mm. These inclusions appear as individual grains or in combination, where pyrite supplants the chalcopyrite (Fig. 6.10).

Pyrite appears in veinlets with irregular shape and 0.5–1 mm thickness as well as in the fractured ore zone, composed of fractured, anhedral-subhedral pyrite grains size of which varies from 0.5 to 5 mm. Micro-cracks between the pyrite grains sometimes are filled by chalcopyrite.

Most part of the fractured ore zone has a porphyric pyrite-magnetite-chalcopyrite texture type, which appears surrounding the large, central quartz grain. The matrix of this ore type is massive pyrite, comprised of 0.2–0.5 mm grains. The pyrite matrix includes anhedral, isometric magnetite grains with size between 0.2–0.7 mm. Massive chalcopyrite appears at the boundary of the magnetite and around fractures among the magnetite grains (Fig. 6.11).
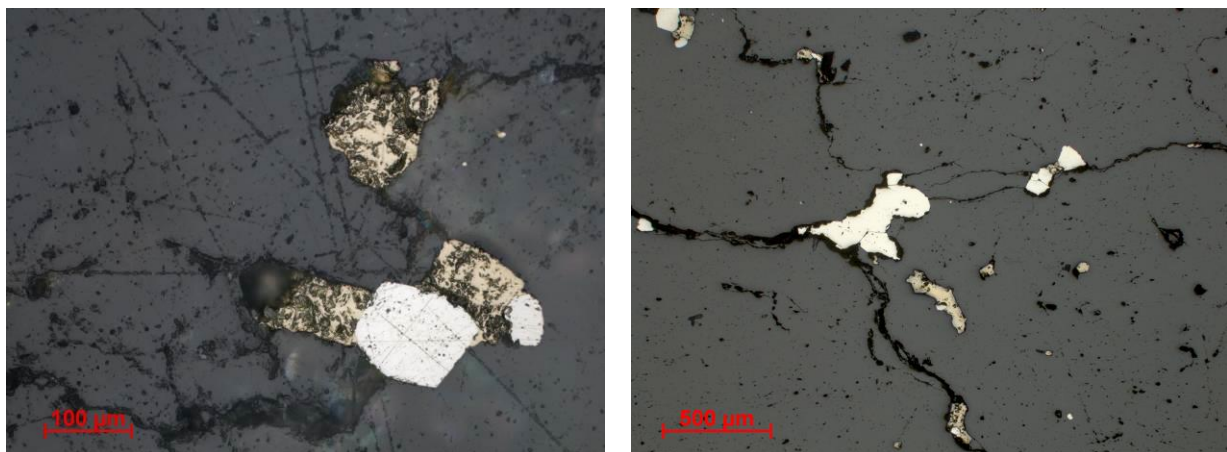

Figure 6.10 Left: Subhedral pyrite crystals (white), supplanting chalcopyrite (yellow) formed in fractures of the quartz aggregate (dark grey) (RL PPL). Right: Anhedral pyrite (white) and chalcopyrite (yellow) grains formed in fractures of the quartz aggregate (dark grey) (RL PPL).

There is one part of the sample (5%) which is strongly fractured and chalcopyrite forms the matrix, embedding the anhedral and subhedral pyrite grains.

These different textures show the intensive fracturing of the rock. First ore mineral, appearing in the fractures was magnetite, followed by chalcopyrite and later by pyrite.

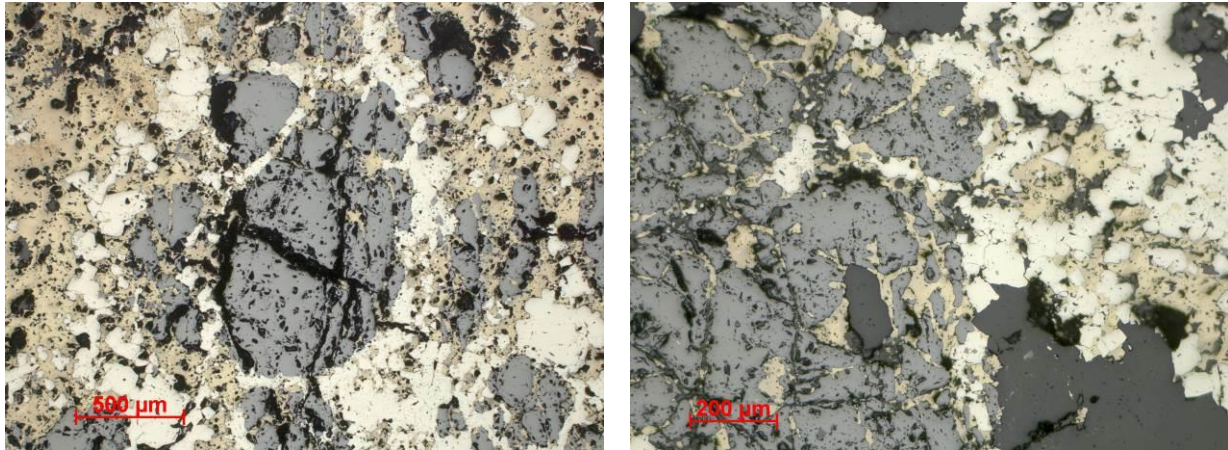*Transmitted light microscopy:* 80% of the sample consists of ore minerals, thin section was not made

Figure 6.11 Left: Anhedral magnetite grains (grey), embedded in the pyrite (white) and chalcopyrite (yellow) matrix (RL PPL). Right: Chalcopyrite (yellow) fills the fractures between magnetite grains (grey). Pyrite (white) occurs in subhedral grains and in aggregate, as the last ore mineral (RL PPL).

Sample 6: Pyrite, chalcopyrite and iron oxide ore

Reflected light microscopy: 80% of the sample is composed of ore minerals. About 40% of the surface of the sample is a massive pyrite aggregate with 2.5–3 mm diameter. The pyrite aggregate is comprised of subhedral crystals with 2–5 mm size. Individual pyrite crystals with the same size are found also, separated from the aggregate. The pyrite is fractured by microcracks with 0.5–2 mm frequency and contains quartz and magnetite-hematite inclusions of 0.1 mm or less (Fig. 6.12 left). Tetrahedrite is also present as an accessory (Fig. 6.12 right).
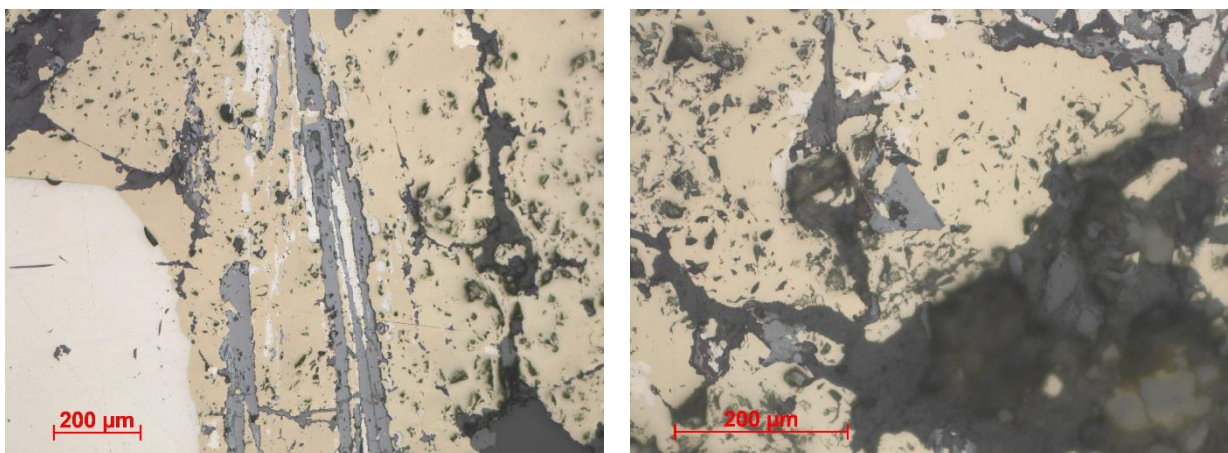
Figure 6.12 Left: Corner of a large pyrite grain with lamellar pyrite and hematite in chalcopyrite (same site as on figure 6.36 right) (RL PPL). Right: Tetrahedrite in chalcopyrite matrix (RL PPL).

The subhedral pyrite aggregate and crystals supplant the chalcopyrite-rich ore. Matrix of the sample is composed of massive chalcopyrite with poikilitic inclusions of, or micrographic intergrowth with quartz

(Fig.6.13 left). Size of the quartz inclusions varies from 0.05 to 1 mm. Tiny (<0.1 mm) anhedral pyrite and magnetite grains appear in the chalcopyrite, usually around boundaries with the quartz.

About 10% of the sample is composed of radially-fibrous aggregates of magnetite-hematite (Fig. 6.13 right). These aggregates appear between the pyrite crystals, supplanting them and at the boundary of the large pyrite aggregate with the massive chalcopyrite. These radial aggregates supplant also the chalcopyrite, which may be found in tiny inclusions among the magnetite-hematite needles.

Transmitted light microscopy: 80% of the sample consists of ore minerals, thin section was not made
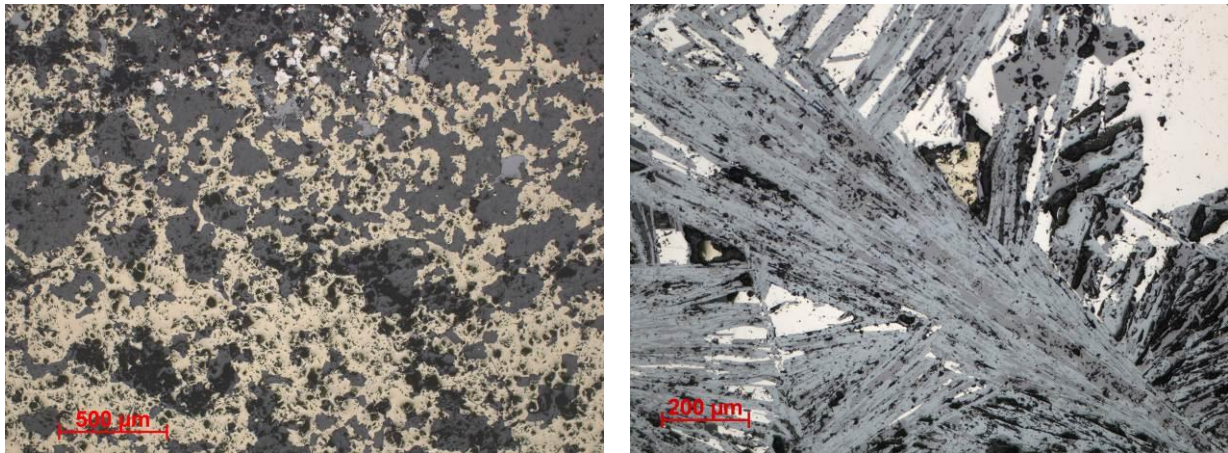
Figure 6.13 Left: Graphic intergrowth of chalcopyrite (yellow) and quartz (dark grey) with disseminated pyrite (white) and magnetite (mid-grey) grains (RL PPL). Right: Fibrous aggregates of magnetite (mid-grey needles) and hematite (bluish-grey needles) supplanting pyrite (white) and chalcopyrite (yellow) (RL PPL).

<u>Sample 7:</u> Pyrite-rich porphyric ore with chalcopyrite

Reflected light microscopy: Euhedral-subhedral pyrite crystals and subhedral chalcopyrite grains appear scattered in the gangue. Pyrite crystals reach a few mm size, while chalcopyrite occurs in 0.2–0.7 mm grains.
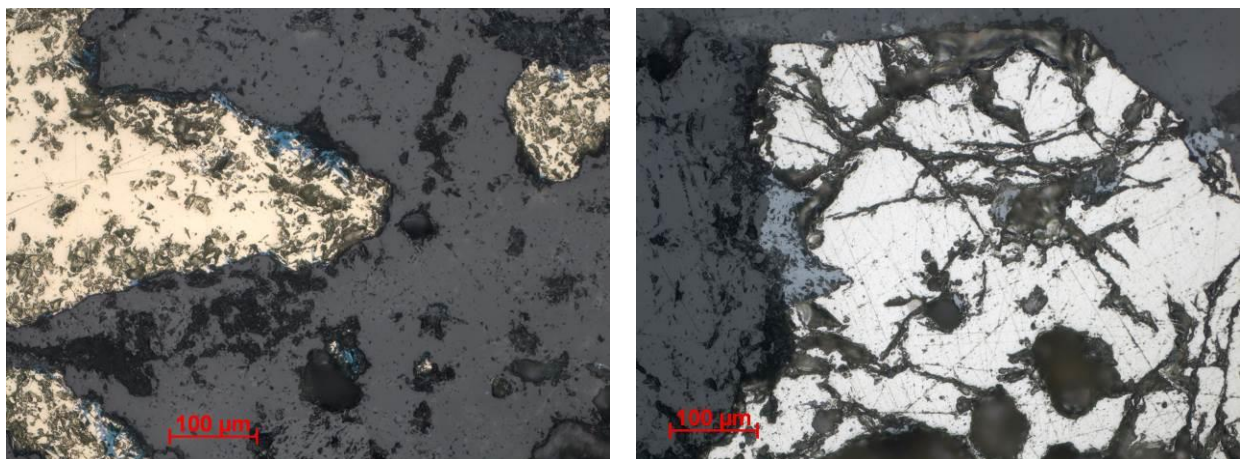
Figure 6.14 Left: Slightly altered chalcopyrite (yellow) with covellite at the boundary (blue) (RL PPL). Right: Shattered pyrite grain (white) with fissures, partly oxidized to hematite (dark grey) (RL PPL).

The sample is moderately weathered. Some pyrite crystals are partly oxidized to hematite and goethite, while covellite occurs at the edge of the chalcopyrite grains (Fig. 6.14). Pyrite grains are often shattered by microcracks, along which the hematite and goethite appears. Sometimes chalcopyrite appears as crack-filling in the shattered pyrite crystals (Fig. 6.15).
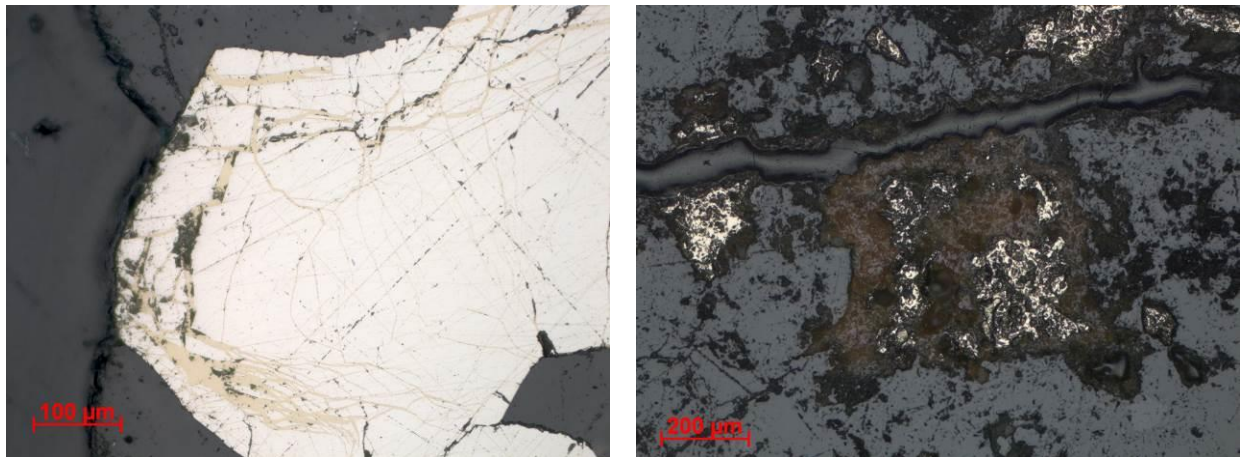
Figure 6.15 Left: Shattered pyrite crystal (white) with chalcopyrite (yellow) in fissures (RL PPL). Right: Heavily corroded pyrite grain altered to goethite (reddish) (RL PPL).

Transmitted light microscopy: Thin section was not made

Sample 20: Moderately weathered pyrite-rich ore with chalcopyrite

Reflected light microscopy: Subhedral pyrite grains with a few mm size appear scattered in the sample, forming clusters from 3–6 grains. Pyrite grains have tiny microcracks with 0.2–0.5 mm frequency. Chalcopyrite and magnetite rims the pyrite crystals at some parts of the sample (Fig. 6.16). Pyrite comprises 15%, chalcopyrite and magnetite appears in 1-2%. Pyrrhotite-chalcopyrite inclusions are found in the pyrite grains. Size of these inclusions is usually below 0.05 mm, sometimes reaches 0.2 mm.

Transmitted light microscopy: The sample comprises ~20 % opaque mineral, ~50 % polycrystalline quartz and ~30 % clinochlore and accessory minerals. The quartz is inequigranular with undulatory extinction and high number of fluid inclusions. The clinochlore is developed as acicular-fibrous aggregates, and fine grained interstitial filling. The chlorite is colourless to pale green (slightly pleochroic) and has anomalous interference colours of pale green attributed to Fe>>Mg content, also segments of dark violet which are dark brown at 1N probably caused by Mn or Ti substitution (Fig. 6.17). Scattered occurrence of muscovite lamellae is also observed, marking a restricted K-mobilisation in the favour of Fe and Mg.
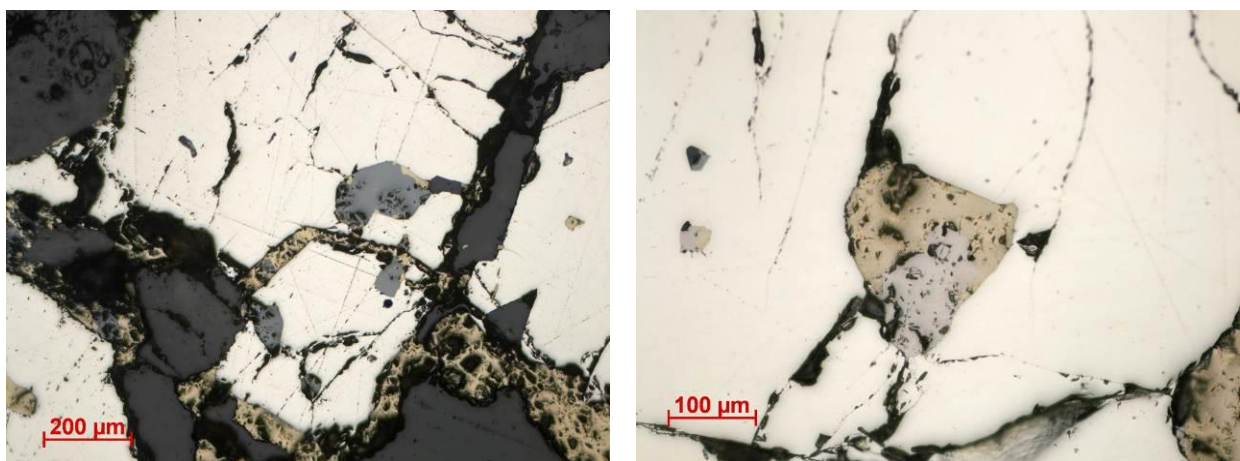

Figure 6.16 Left: Pyrite crystals (white) rimmed by chalcopyrite (yellow) with magnetite inclusions (dark grey) (RL PPL). Right: Pyrite grain (white) with inclusions of pyrrhotite (rose-grey) and chalcopyrite (yellow) (RL PPL).
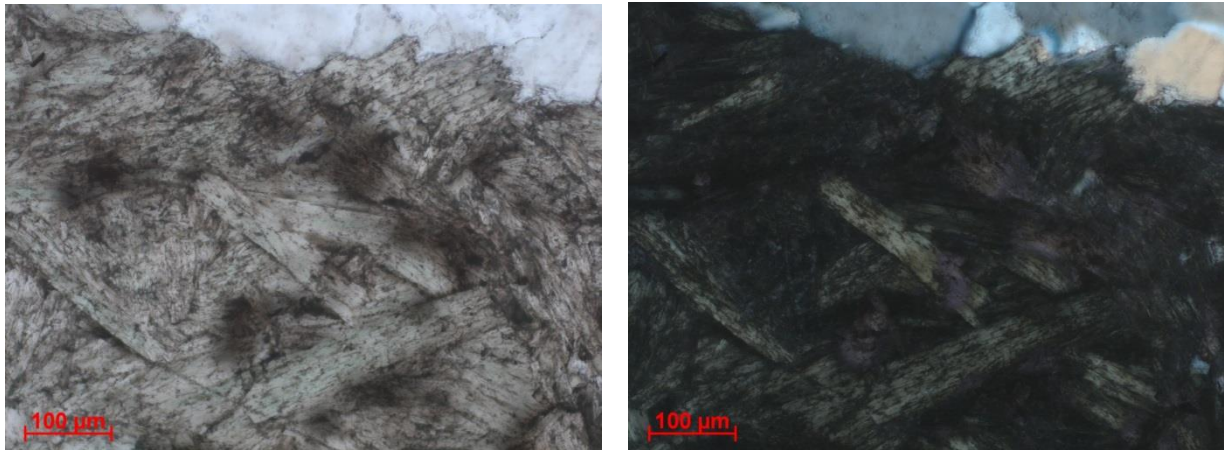
Figure 6.17 Pleochroic chlorite with variable interference colours (TL PPL and XPL).

6.3.5 Texture group 5: Porphyric pyrite-magnetite ores

Three skarn samples were classified in this group:

• Sample 12: pyrite-magnetite skarn ore with chalcopyrite

• Sample 13: pyrite-magnetite skarn ore with chalcopyrite

• Sample 14: pyrite-magnetite skarn ore with chalcopyrite

<u>Sample 12:</u> Skarn pyrite-magnetite ore

Reflected light microscopy: The sample is a massive pyrite ore sample with highly complex texture. Other ore minerals present are magnetite, chalcopyrite and hematite.

Main part of the sample is composed of massive pyrite, in many parts fragmented by oxidation-exsolution zones of magnetite developed interstitially around pyrite.

Massive pyrite in many parts contains lamellar zones with nearly the same reflection intensity and slightly bluish colour, reaching 50–100 μm length and 10–30 μm width (Fig. 6.18 left). First it was interpreted as arsenopyrite lamellae in the pyrite, but arsenopyrite was not detected by XRPD or microprobe. Scanning microprobe show that these lamellae are also composed of pyrite, but it is not excluded that they are contaminated with very low silver content (?).

These lamellae are sometimes rimmed by elongated magnetite, formed by oxidation-exsolution of pyrite (Fig. 6.18 right). Magnetite appears in anhedral patches within the pyrite and in other parts as zones rimming the pyrite. The frequency of exsolution is very changeable. There are parts, composed of massive pyrite reaching few mm-s, then parts with pyrite grains of 10–50 μm and other parts where exsolution takes place in submicron size range. The pyrite-dominant massive ore is surrounded by calcite grains of 3–5 mm size. At the rim of the pyrite ore, sulphosalts (tetrahedrite-tennantite?) and chalcopyrite appears in anhedral flakes and grains developed along 10–30 μm long microcracks. Sometimes patches of sulphosalts with sphalerite and chalcopyrite appear also in the massive ore (Fig. 6.19 left).

Transmitted light microscopy: Coarse-grained dolomite appears in cavities of the massive pyrite-magnetite ore. Texture of the carbonate is polygonal, formed by contact metamorphism from carbonate grains (Fig. 6.19 right). At the edge of the massive ore, coarse-grained dolomite forms the matrix, having tiny magnetite inclusions along the grain boundaries.
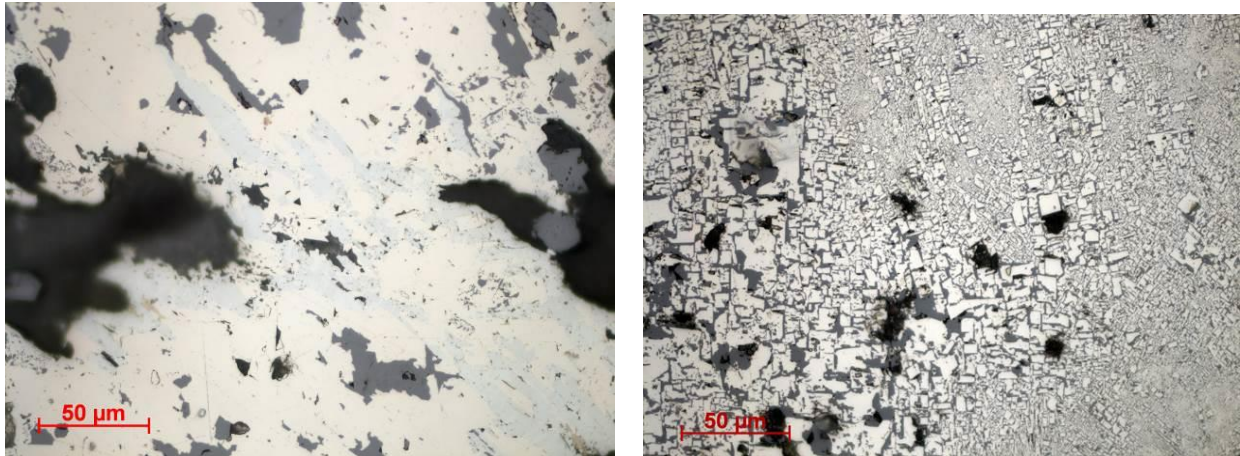
Figure 6.18 Left: Massive pyrite (creamy with bluish lamellae) and patches of magnetite (dark grey) (RL PPL). Right: Pyrite-magnetite exsolution with very variable size range (RL PPL).
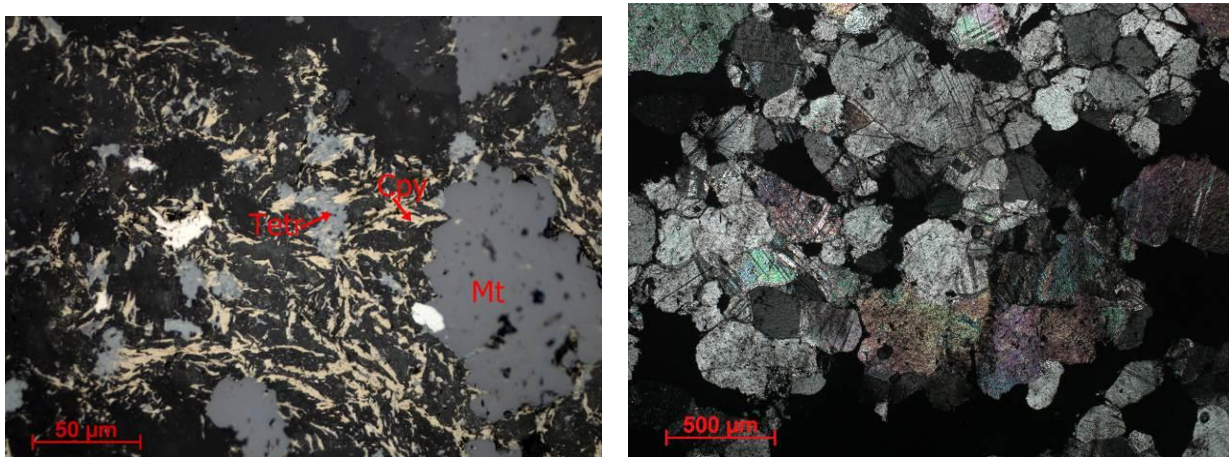

Figure 6.19 Left: Anhedral chalcopyrite (yellow) and tetrahedrite-tennantite (mid-bluish gray) masses developed along microcracks in calcite (dark) (RL PPL). Right: Polygonal texture of coarse-grained carbonate rock, resembling to contact marble (TL XPL).

<u>Sample 13:</u> Skarn pyrite-magnetite ore

Reflected light microscopy: Ore minerals appear in the sample as late phases of precipitation, filling anhedral and angular cavities left after crystallization of silicates and carbonates. Main mass of the ore is composed of pyrite, including the same slightly bluish lamellae as it was found in sample 12 (Fig. 6.20). The lamellae have 10–30 μm width and extend to 100 μm length. These lamellae usually develop along cracks in the pyrite, mainly subparallel to the cracks but also at high angle. Cracks are usually filled by hematite. Forming graphic texture, pyrite includes magnetite and hematite exsolution zones, appearing in different frequency: from 100–200 μm to submicron size.

Sometimes pyrite contains pyrrhotite and chalcopyrite grains near the boundaries with gangue minerals.

Transmitted light microscopy: The matrix of the sample is colourless, isotropic material, with local anisotropy developed as lamellar pattern. Calcite like fissure filling material is observed. Hypidiomorphic and anhedral pyroxene (diopside?) crystals are developed associated to opaque minerals and low birefringence-low relief lamellar products, probably "hidrogarnet". Opaque components are developed as stock-work of pyrite (anisotropy to dark blue may indicate chemical substitutions). Sphalerite (medium grey, isotropic) and magnetite (grey, isotropic) inclusions are frequent at < 10 μm size, hematite (light grey, red at xN) is

developed on expense of magnetite. Chalcopyrite (yellow, greenish at xN) of ~10 μm is present in relict, etched crystals. Associated to suplhide cementing material, euhedral augite and diopside crystals are developed. Veinlets have pyrite filling, oxidized to "limonite". Relicts of euhedral garnets with anisotrophy developed in lamellae are observed, with nodules of pyrite + sphalerite replacement.
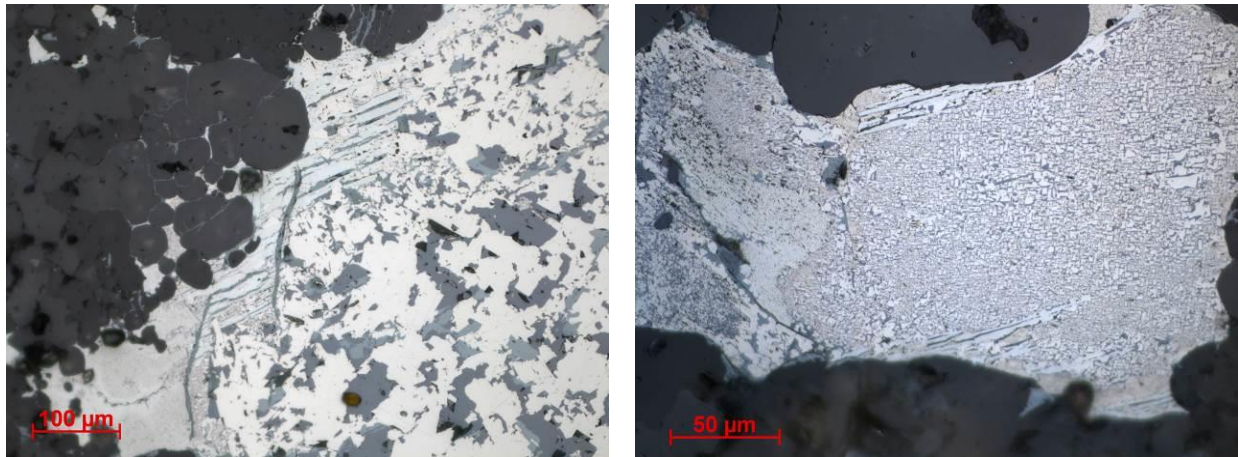

Figure 6.20 Left: Massive pyrite (white with bluish lamellae) with magnetite-hematite inclusions (dark / mid grey) (RL PPL); same area as on figure 6.39 right. Right: Fine-grained dissolution of pyrite (white) and magnetite (dark grey) (RL PPL).

<u>Sample 14:</u> Skarn pyrite-magnetite ore

Reflected light microscopy: This sample resembles to specimens No 12 and 13 but there are differences. Pyrite grains form masses with cm-size, intergrown with acicular-fibrous crystals and inclusions of the gangue minerals. Pyrite in this sample has the same light bluish lamellae as in samples 12 and 13 in the massive pyrite grains (Fig. 6.21). There is another pyrite mass, having elongated structure, which was formed by replacing original mafic (actinolite by XRPD) mineral grains. Very few chalcopyrite grains develop at the boundary of fractured pyrite.
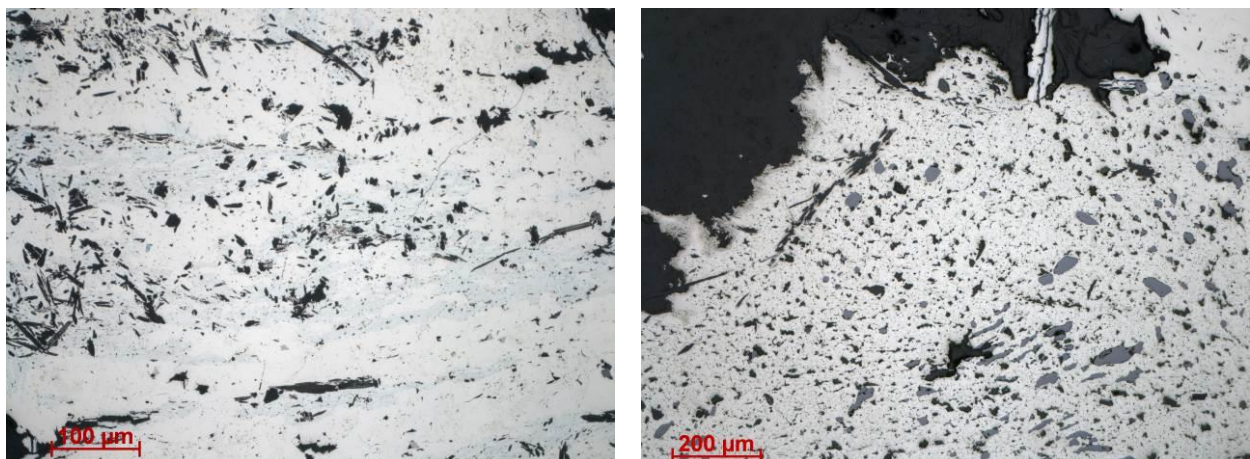

Figure 6.21 Left: Massive pyrite (white with bluish lamellae) with inclusions of acicular grains. (RL PPL). Right: Massive pyrite (white) with oval inclusions of magnetite (dark grey) (RL PPL).

Transmitted light microscopy: The sample is made up by a stockwork of opaque minerals associated with grainy green and yellow groundmass, presumably the alteration product of the host rock, built up by colourless, anhedral, strongly reacted grains. The matrix is built up by fine grained colourless material, with interference colours of tremolite. The yellow – pleochroic in pale yellow – and green – pleochroic in green –

grains are also amphiboles, assumed to be Fe-bearing tremolite and actinolite. Anhedral isolated quartz grain are also observed. The opaque mineral is pyrite, with amphibole inclusions. In the matrix some relics of anhedral grains with serpentine minerals are observed. Larger nodules of polycrystalline quartz with amphibole inclusions are characteristic. Veinlets of sanidine are developed (Fig. 6.22). Opaque fraction (~10%) is exclusively pyrite, with only a few small grains resembling chalcopyrite.
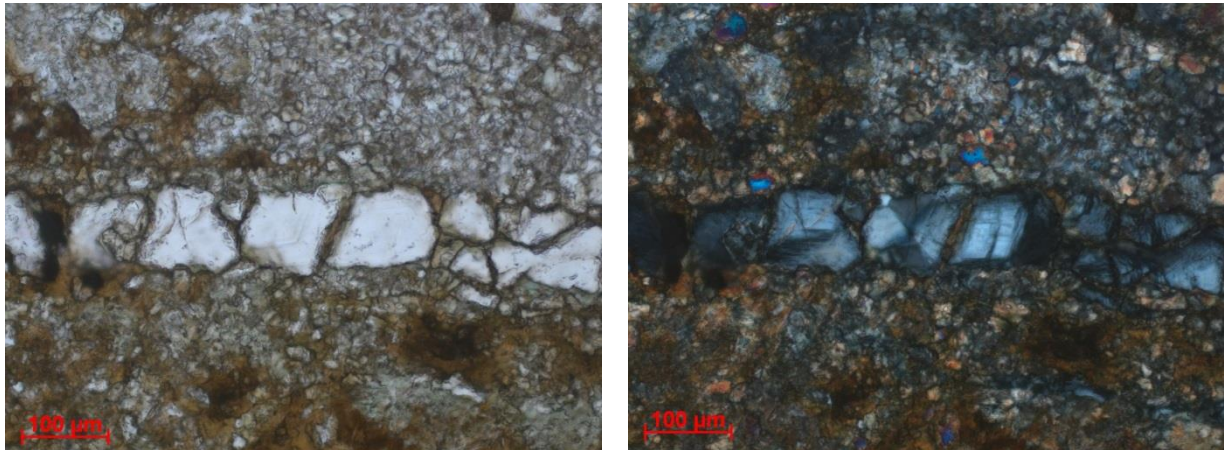
Figure 6.22 Sanidine vein in amphibole matrix (TL PPL and XPL).

6.3.6   Texture group 6: Banded massive ores

Five samples were classified in this group, two ore and three country rock samples which supplement the Corvo VMS ore:

• 4: baritic Pb-Zn ore

• 26: VMS Cu-Zn-Sn ore

• 23, 24, 25: volcanics of the IBERIAN PYRITE BELT
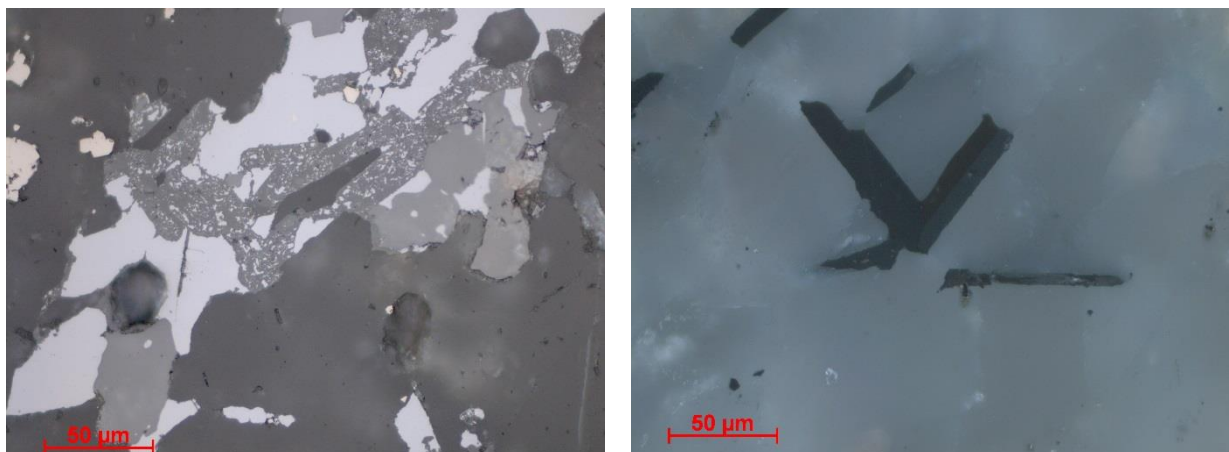
Sample 4: baritic Pb-Zn ore

Figure 6.23 Left: Galena (bright, partly altered to grey cerussite) and sphalerite (grey) in barite matrix (dark grey) with pyrite grains (RL PPL). Right: Galena (isotropic, dark) and geocronite (anisotropic, grey) in barite matrix (RL XPL).

Reflected light microscopy: The sample has a banded texture with variable proportions of barite, quartz and ore minerals. Pyrite and galena-sphalerite assemblages often form fragments embedded in barite. Patchy masses of galena partly altered to cerussite also fill the voids of the barite (Fig. 6.23 left). Galena is in some places associated with an anisothropic, typically fibrous sulphosalt (geocronite according to EDX measurements) (Fig. 6.23 right).

Transmitted light microscopy: The sample comprises dominantly inequigranular polycrystalline barite (~70 %), calcite (~10 %) and opaque minerals with translucent opacitized phases (~20 %) (Fig. 6.24). "Limonitic" patches in the calcite enriched parts consist of goethite. Minor amount of disseminated muscovite lamellae are characteristic.
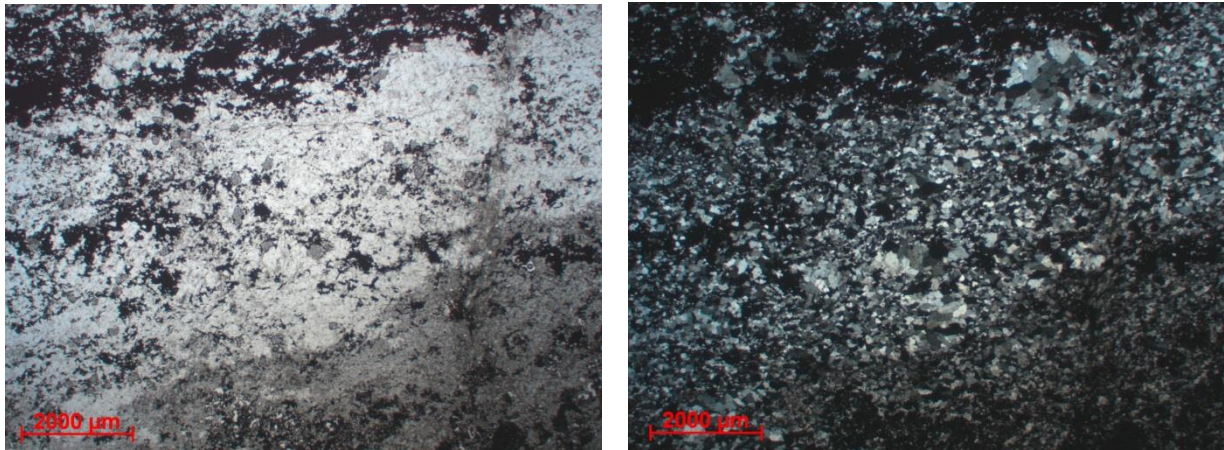

Figure 6.24 Transparent barite matrix with translucent and opaque grains; bands of different grain size and proportions of these minerals (TL PPL and XPL).

<u>Sample 26:</u> massive stratiform chalcopyrite ore with pyrite and sphalerite

Reflected light microscopy: The sample has a layered texture. Characteristics of the layers change by 2–3 mm. Main minerals are chalcopyrite, pyrite and sphalerite. In some parts cassiterite appears as well.
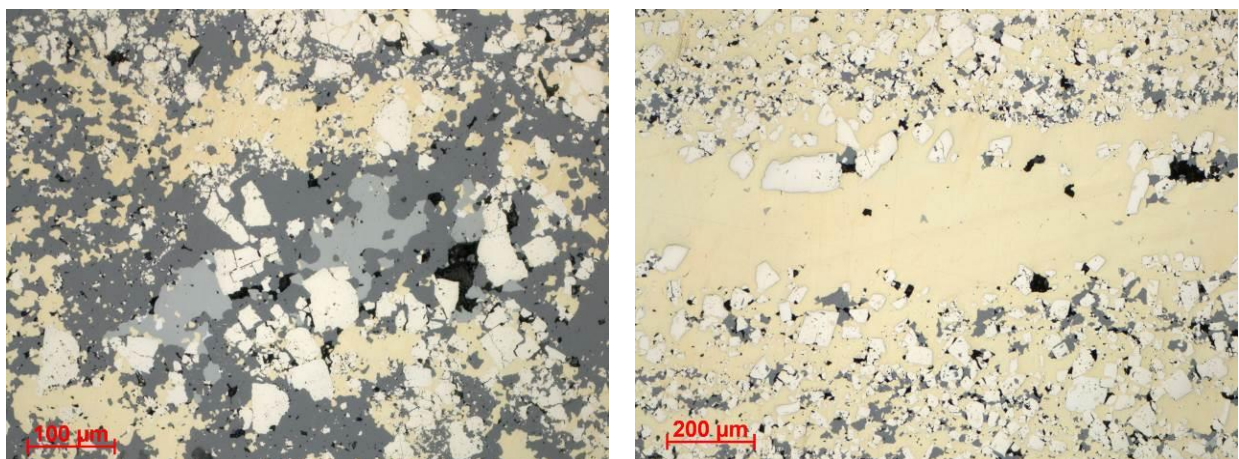

Figure 6.25 Left: Subhedral and anhedral pyrite grains (white) in the sphalerite (dark grey) and chalcopyrite (yellow) matrix. Middle part of the sphalerite contains anhedral mass of cassiterite (RL PPL). Right: Subhedral and anhedral pyrite grains (white) in the chalcopyrite (yellow) matrix with little sphalerite (dark grey) (RL PPL).

Chalcopyrite is the dominant mineral in the sample and forms the groundmass in most of micro-seams. Grains of chalcopyrite cannot be distinguished. In other micro-seams the groundmass is partly or mostly

replaced by sphalerite, which appears in general as masses. There is one micro-seam where isometric or prismatic crystals of sphalerite are partially replaced by chalcopyrite, forming a very fine-grained sieve texture.

Appearance of pyrite is manyfold. It usually forms individual anhedral or subhedral grains from a few micrometers size till 0.2–0.3 mm. Large (0.2–0.3 mm) pyrite grains are rounded and the texture shows rotation of these grains in the fine-grained groundmass. Even larger pyrite grains (up to 1 mm) had been shattered and the voids between the fragments are mainly filled up by sphalerite. There are seams where pyrite is fine-grained (few micrometers) and anhedral, while in another seam it forms euhedral-subhedral crystals of 0.05–0.1 mm.

There was one seam found where small (up to 0.1 mm) anhedral masses of cassiterite appear inside the sphalerite (Fig. 6.25).

Transmitted light microscopy: Massive ore, thin section was not made.

Sample 23: metasomatic felsic volcanic rock

The sample is Ca-metasomatised felsic rock, the rounded quartz grains indicate sedimentary or volcanoclastic origin. Thin veinlets of muscovite with minor biotite component are cross-cutting the texture. The matrix is a mixture of fine grained quartz and intermediary plagioclase with prismatic-acicular habit. Calcite veins of twinned anhedral crystals contain ~10 µm sized chalcopyrite grains, hematite is developed on the expense of pyrite or magnetite. In the matrix anhedral to subhedral ilmenite grains are observed, occasionally with anatase rim, associated mainly to muscovite veinlets with euhedral orthoclase crystals (Fig. 6.26). Also a relict of a strongly sericitized plagioclase phenocrystal is observed. Coarse grained apatite occurs in euhedral crystals as accessory component.
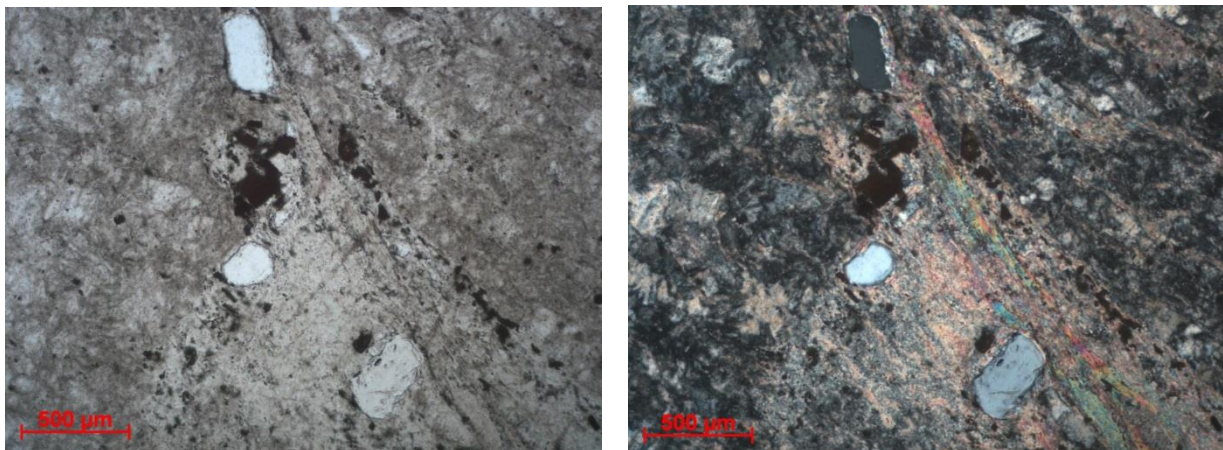

Figure 6.26 Euhedral orthoclase grains in muscovite matrix with a sericitized relict of a plagioclase in the middle (TL PPL and XPL).

Sample 24: cataclastic felsic volcanic rock

Cataclastic rock with high acidic plagioclase, sericite and quartz content, formed by hydrothermal fragmentation of previously metasomatized volcanics. Large porphyroblasts containig chlorite flakes, plagioclase crystals often calcitized and quartz are isolated by microcrystalline quartz-sericite matrix. Chlorite flakes are pseudomorph-like and interference colour suggests Mg>>Fe content, probably by the alteration of hornblende. Nodules of prismatic plagioclase crystals indicate the transformation by devitrification of volcanic glass, calcite is developed as pore filling component. Monazite is a common accessory mineral, in

crystal groups or nodules of some hundreds of micrometers (Fig 6.27). In the fine grained plagioclase-quartz dominated texture calcite veins are frequent. Opaque fraction (<1 %) is pyrite in magnetite.
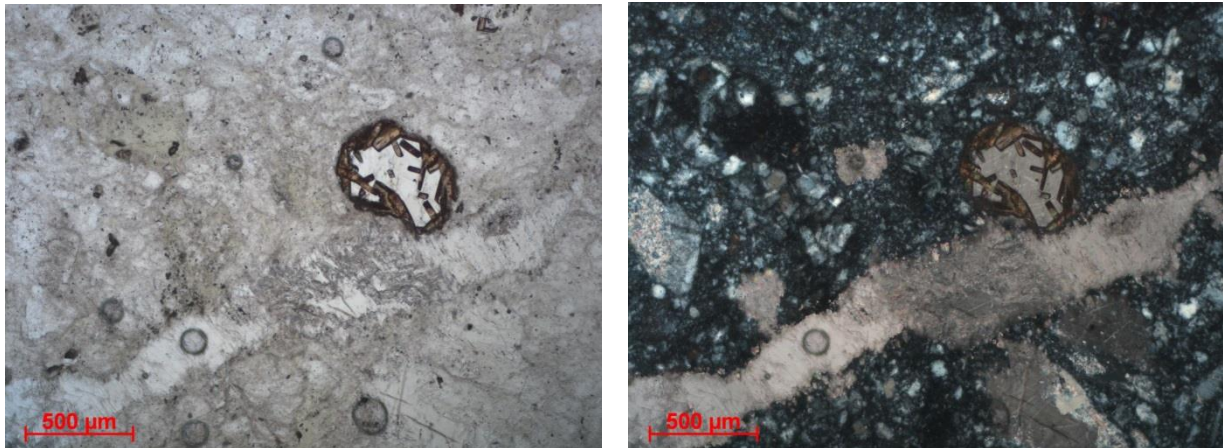

Figure 6.27 Monazite assemblage on the rim of a porphyry quartz grain in glassy matrix with calcitized plagioclase grains (TL PPL and XPL).

<u>Sample 25:</u> cataclastic felsic volcanic rock

Strongly altered and calcitized clastic rock with relicts of plagioclase phenocrystals replaced by calcite. Calcite vein are characteristic, the matrix is composed of quartz, plagioclase, sericite and clinochlore with patches of calcite. The chlorite grains in the matrix have an oxidation rim consisting of "limonite" and probably anatase. The original plagioclase crystals were prismatic, idiomorphic, alteration was developed as zoning of calcite and sericite rich rims (Fig. 6.28). Pyrite is associated to thin chloritic-sericitic veinlets overgrown by later calcite veins.
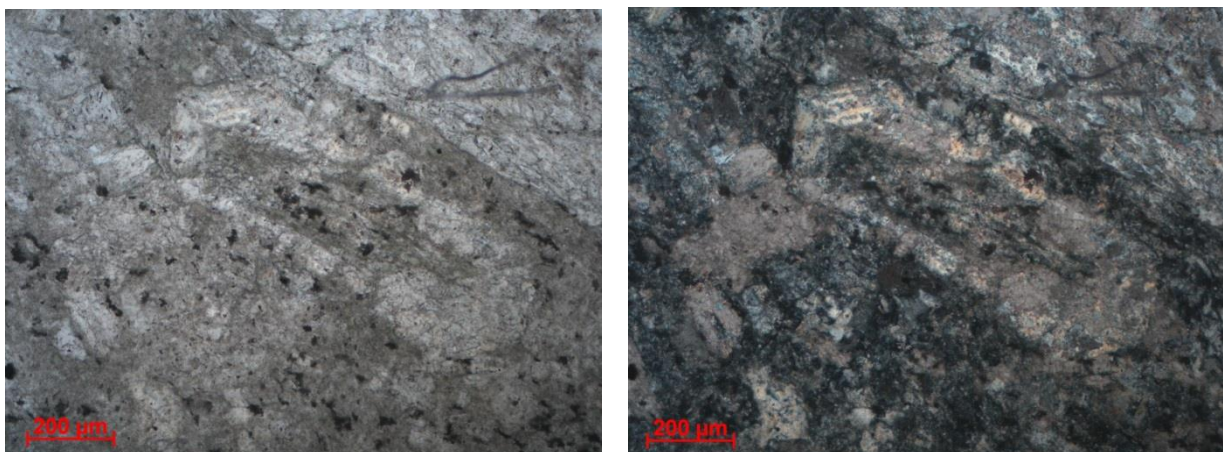

Figure 6.28 Relict of a plagioclase crystal replaced by calcite and sericite (TL PPL and XPL).

6.3.7   Non-classified samples

Three samples have different texture and were not classified in the above or other groups.

<u>Sample 3:</u> Vein-type polymetallic ore

Reflected light microscopy: The sample is a part of a vein of 5–10 cm thickness, filled zonally. The sample shows the central zone with weak (10–15%) sphalerite and galena content, followed by the zone of polymetallic (pyrite, chalcopyrite, galena, sphalerite) ores, then by a zone of coarse-grained calcite, supplanting a zone of fine-grained calcite with disseminated pyrite.

The central zone is composed of a fine-grained (<0.1 mm) quartz and calcite (0.1–0.3 mm) matrix. This matrix includes the subhedral sphalerite crystals that reach 0.3–0.5 mm size (Fig. 6.29). Galena and pyrite appear in the fissures of the vein, sometimes in the micro-cracks of the sphalerite as well.

The polymetallic zone has a carbonate matrix of 0.1–0.2 mm grains. Ore grains are found disseminated in the matrix, comprising 5-10%. Chalcopyrite appears in tiny (0.1–0.3 mm), subhedral crystals with pyrite inclusions in the core. Sphalerite appears in the same size range at the boundary of the chalcopyrite, often supplanting it. The coarse-grained (5–8 mm) calcite is pure, does not contain ore minerals.

Transmitted light microscopy: The central zone is composed of elongated, fine-grained (<0.05 mm) quartz and carbonate, embedding the subhedral sphalerite crystals (fig. 6.30). The matrix of the second zone, bordering the central zone contains carbonate grains of different size (0.05–0.5 mm). This zone has a dark brown colour, probably due to Fe contamination of the carbonate. XRPD detected kutnohorite from the sample. The coarse-grained calcite zone is composed of 2–3 mm crystals with perfect grain boundaries, along which these crystals supplant the microcrystalline (0.1–0.2 mm) carbonate-pyrite mass.
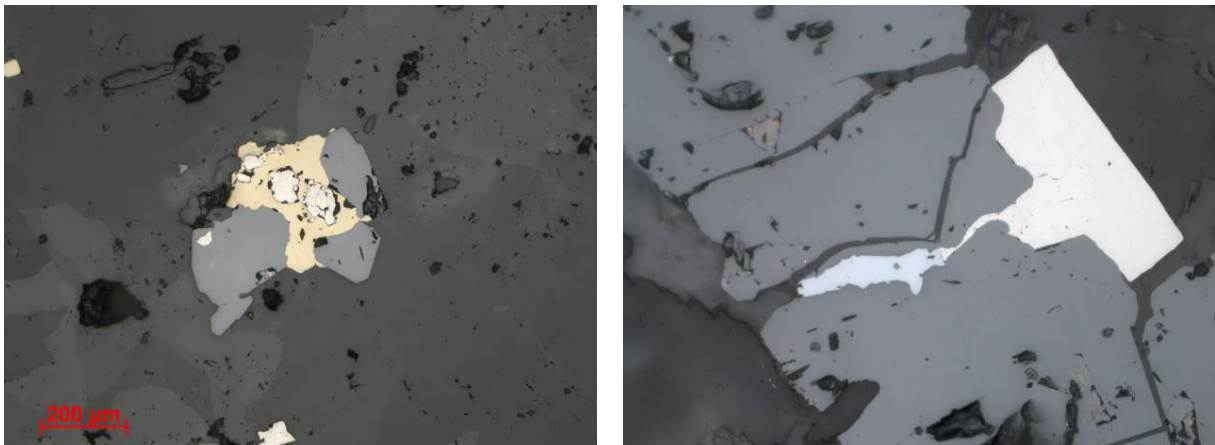

Figure 6.29 Left: Polymetallic zone: anhedral sphalerite grains (mid-grey) supplanting chalcopyrite (yellow) which has pyrite inclusion in the core (white) (RL PPL). Right: Central zone: coarse-grained sphalerite (darker grey) with galena (bluish mid-grey) and pyrite (whitish) appearing in the fissure of the sphalerite (RL PPL).
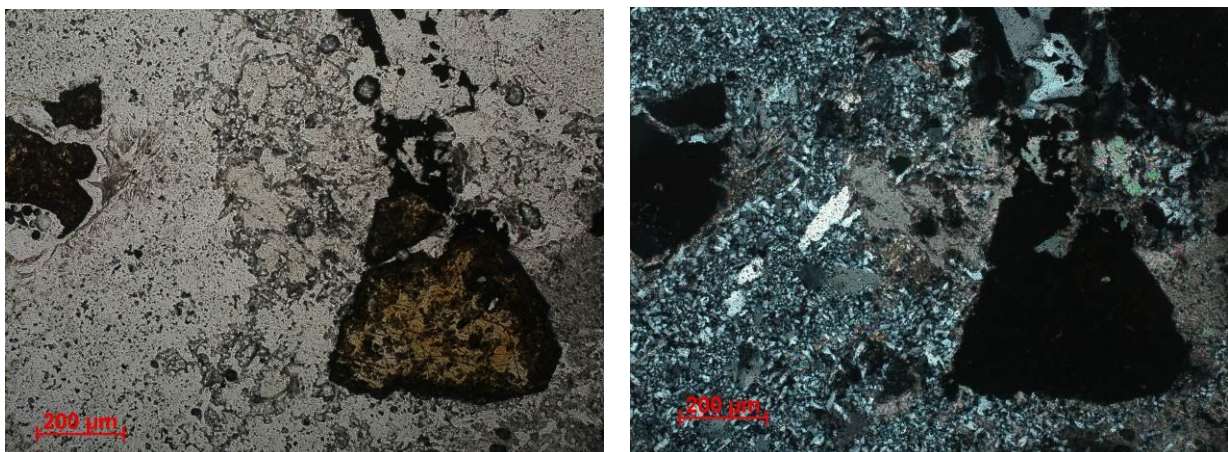

Figure 6.30 Texture of the central zone: fine-grained quartz and carbonate matrix, embedding subhedral crystals of sphalerite. Left: transparent: quartz and calcite, brownish crystals: sphalerite (TL PPL). Right: white-grey fine-grained: quartz, pearly: carbonate, black: sphalerite (TL XPL).

Sample 16: banded iron ore with disseminated magnetite

Reflected light microscopy: Ore minerals are composed dominantly of magnetite. Along microcracks and grain boundaries sometimes hematite occurs with irregular shape or tiny (few micrometers) anhedral inclusions (Fig. 6.31. left).

Magnetite grains have 0.4–2 mm size, they are intensively cracked (by 0.1–0.3 mm) and have inclusions of a few μm size.

Transmitted light microscopy: Magnetite-rich patches develop on the contact zone of carbonate rock and microcrystalline quartz veinlets. The carbonate rock has a microcrystalline texture with anhedral grains of 0.05–0.1 mm. In the contact zone of the carbonate and the quartz veinlet, masses of columnar-prismatic Ca-silicate minerals develop with very low birefringence (Fig. 6.31. right).
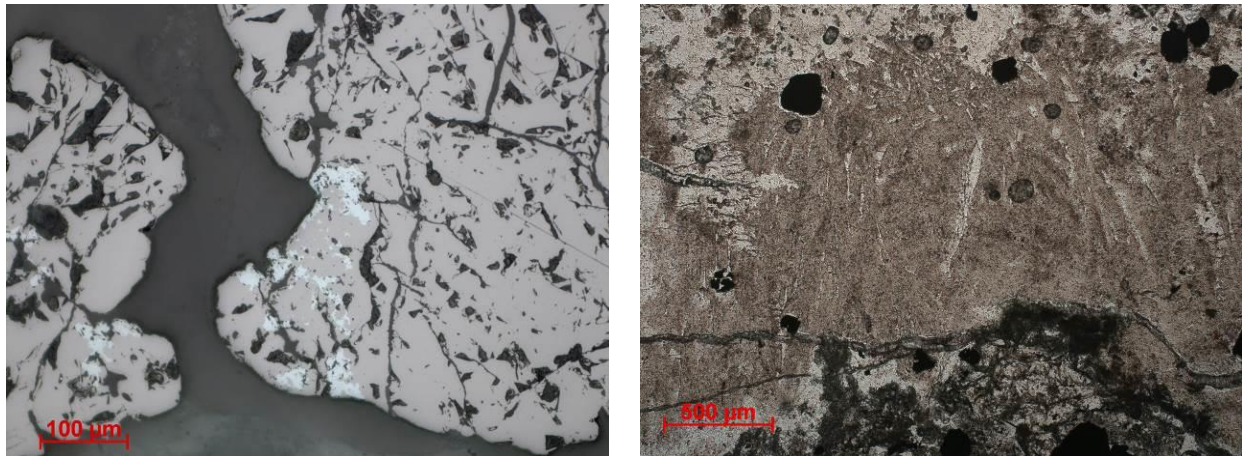

Figure 6.31 Left: Anhedral magnetite grains (mid-grey) with hematite inclusions (lighter bluish grey) (RL PPL). Right: Columnar Ca-silicate minerals in the contact zone of limestone and quartz veinlet (TL PPL).

Sample 21: disseminated pyrite-chalcopyrite ore, Kristinebergsgruvan

Reflected light microscopy: This sample contains subhedral-anhedral grains of pyrite reaching 0.1–0.2 mm disseminated in the gangue (Fig. 6.32). Pyrite comprises ca. 15% of the sample. Pyrite grains often connected by anhedral masses composed of chalcopyrite and magnetite. Chalcopyrite grains are intensively fractured, it was not possible to make a good quality polished section to examine it in detail.
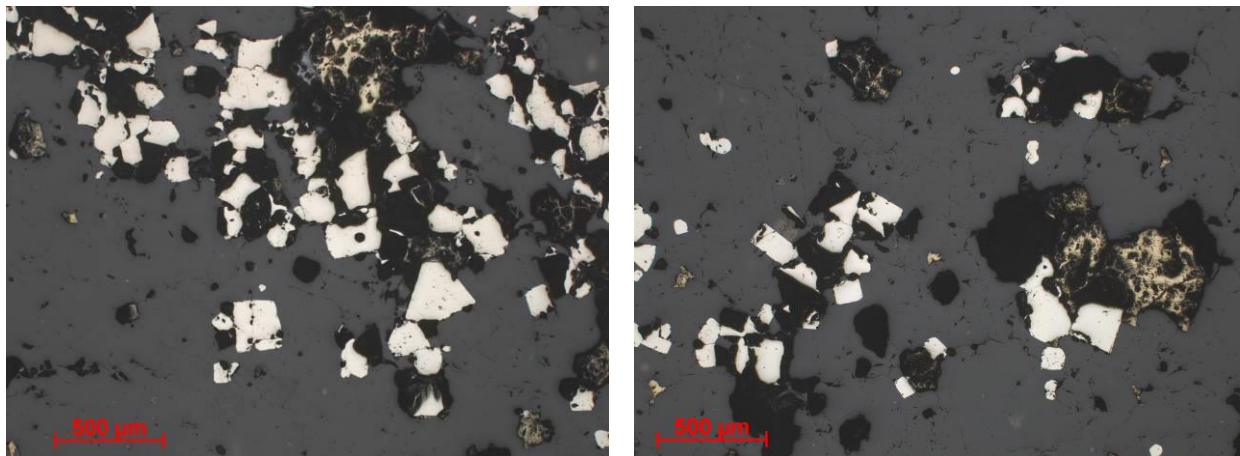

Figure 6.32 Subhedral and euhedral pyrite grains (white) interconnected by chalcopyrite (yellow) and magnetite (dark grey) grains. (RL PPL).

Transmitted light microscopy: The sample is a hydrothermal quartzolite with ~12% chalcopyrite and ~10 % of pyrite. Quartz is polycrystalline, inequigranular, developed in several generations. The smaller grains are developed linked to idiomorphic-hypidiomorphic pyrite cubes, often distorted. Euhedral apatite inclusions are developed in quartz. Lamellae of muscovite and grainy biotite or chlorite are characteristic associated to pyrite, developed interstitially in the opaque grains. Fine lamellar to prismatic fan-displaced crystal groups of pumpellyite are also observed.

6.4 Electron microprobe and EDX measurements

A JEOL JXA-8600 Superprobe electron microprobe with upgraded SAMX control system (15–20 kV, 20 nA, PAP correction) was used for the measurements. Those samples were chosen for measurements only, where optical microscopy, XRD and XRF results indicated problems in mineral identifications which could be solved by this method. Textures are shown on backscattered electron (BSE) images. Compositions were measured without standards. Elements included by the minerals can be detected reliable only if their concentration exceeds cca. 0.1%–0.5%.

Sample 3

The matrix of the sample is quartz and calcite. Calcite contains some percents of Fe, Mn and Mg in inhomogeneous distribution, causing stained appearance on BSE images. Cracks are often filled by clay minerals. Oldest sulphide minerals are pyrite grains (pentagonal in some cases), then chalcopyrite, sphalerite and (less common) galena forms some 10 μm magnitude, anhedral grains, finally disseminated arsenopyrite overprints the earlier grains, forming coatings around them (Fig. 6.33).
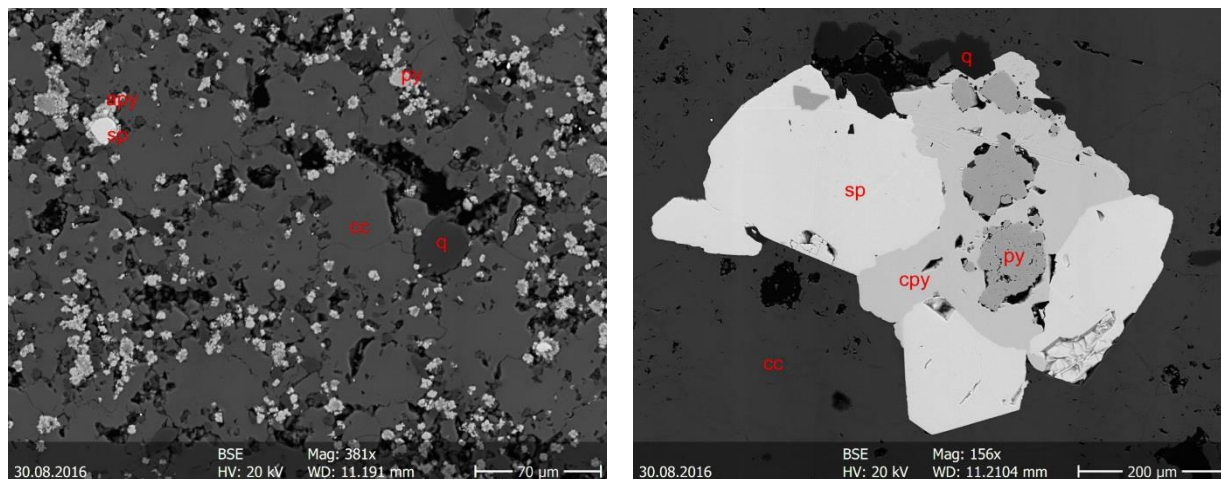

Figure 6.33 Left: disseminated arsenopyrite (apy) in calcite (cc) matrix, grown over pyrite (py), sphalerite (sp) and quartz (q). Right: Fe-containing sphalerite and chalcopyrite grown over pyrite in calcite matrix.

Sample 4

The matrix of the sample is banded, comprising either barite with embedded quartz and sulphide grains or quartz with mica and clay minerals, barite and pyrite. Sulphide minerals are pyrite, sphalerite, galena and geocronite (a Pb-Sb sulphosalt) (Fig. 6.34). Fragments of bacteriopyrite, sometimes associated with sphalerite are relict assemblages in the barite bands (Fig. 6.35). In several places secondary carbonate or sulphate minerals are associated with the primary sulphides as oxidation products (cerussite and bindheimite with galena and geocronite, smithsonite with sphalerite). Limonite also occur containing Pb and Zn.
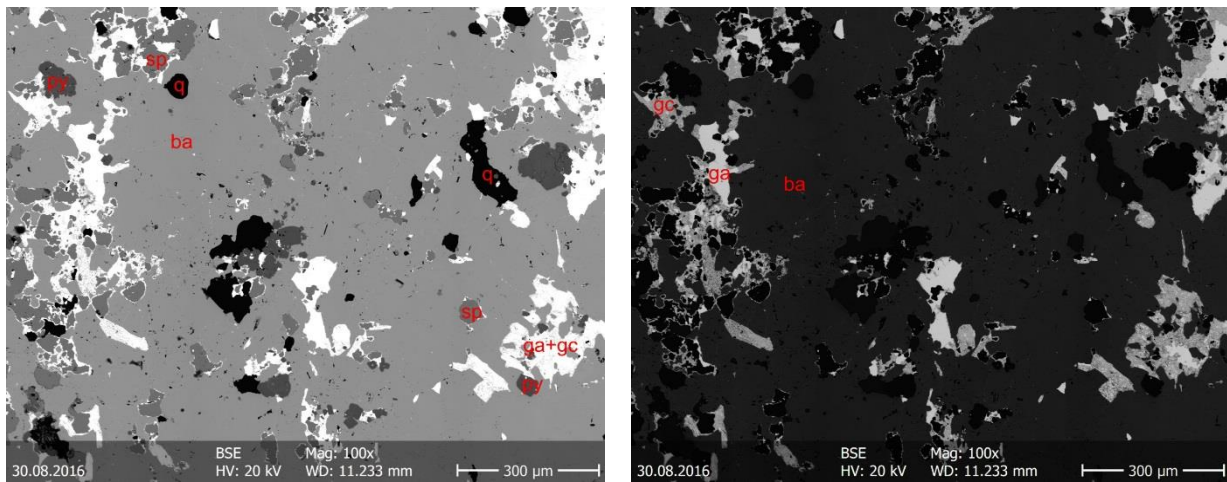
Figure 6.34 Barite matrix with sulphides; the same scene with changed contrast on both sides. Order of brightness: quartz (q), pyrite (py), sphalerite (sp), barite (ba), geocronite (gc) and galena (ga).
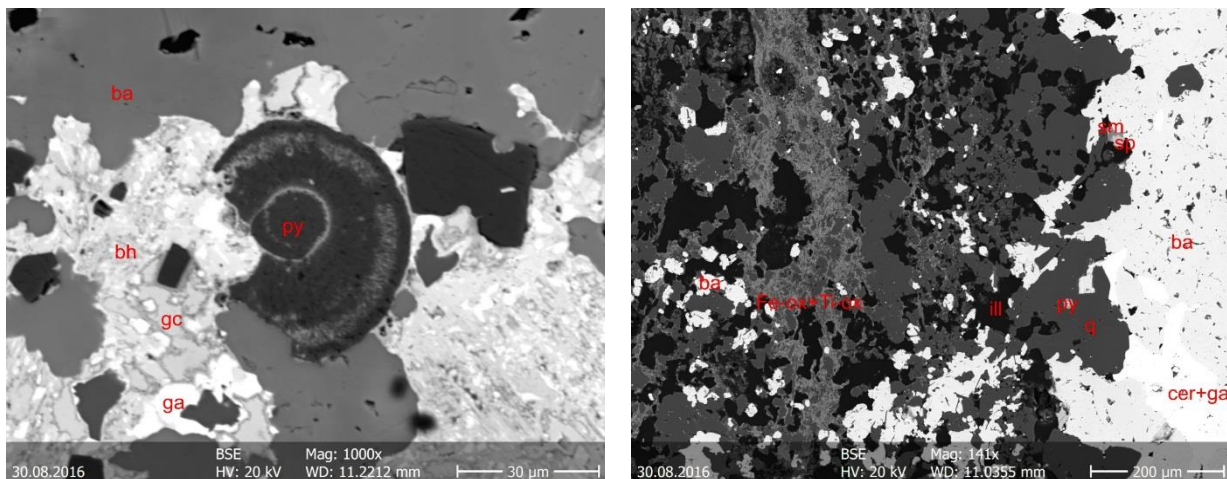

Figure 6.35 Left: concentric bacteriopyrite (py) fragment embedded in barite (ba) matrix, overgrown by galena (ga) and geocronite (gc) (also inside pyrite rings). Bindheimite (bh) occurs as an alteration product of the lead sulphides. Right: boundary of a barite and a quartz dominated band. Barite (ba) contains galena (ga) and cerussite (cer), an alteration product of galena; sphalerite (sp) and smithsonite (sm) also occur at the edge in a similar relation. Quartz (q) is vuggy (black patches) filled partly with micas and illite (ill), barite, some pyrite (py) and a vein of iron and titanium oxides.

Sample 6

The bulk of this sample consists of chalcopyrite and pyrite. Non-sulphide minerals are represented by acicular actinolite (with variable iron content), isometric grains of a Ca-Al-Fe garnet (in composition between andradite and grossular), some diopside and two types of iron oxide. One of these is anhedral and isometric, possibly magnetite, the other, possibly hematite, forms typically fibrous or lamellar, fan-shaped assemblages together with pyrite, sometimes also with chalcopyrite (Fig. 6.36). Rare molybdenite was also found.
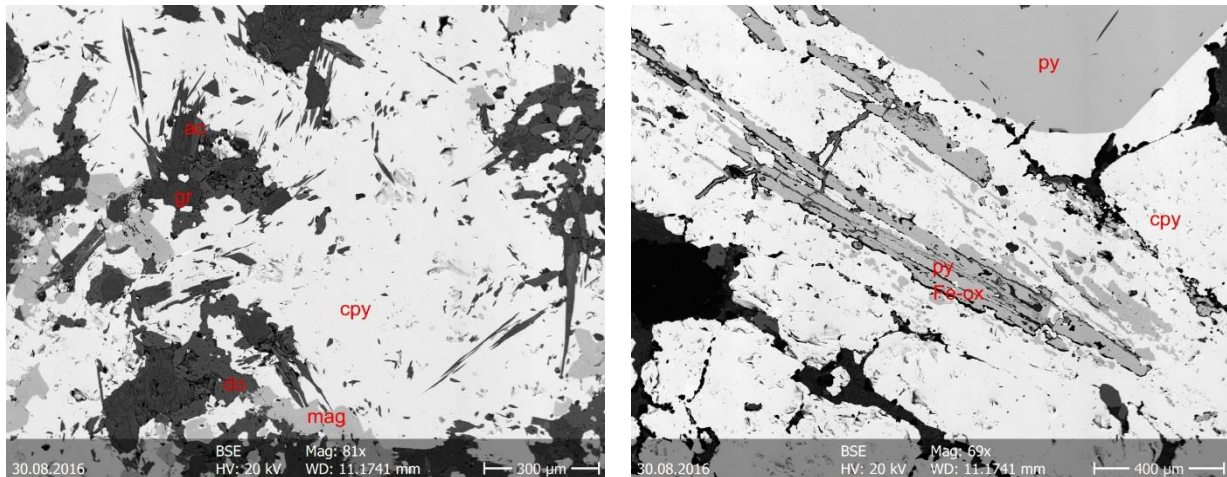
Figure 6.36 Left: chalcopyrite (cpy) with magnetite (mag), actinolite (ac), diopside (do) and garnet (gr). Right: corner of a large pyrite (py) grain with chalcopyrite (cpy) containing lamellar pyrite (py) and iron oxide (hematite?) (same site as on figure 6.12 left).

Sample 9

This sample comprises two parts, a dark lens-like inclusion within a white host. The matrix of the host is calcite and epidote, which contains disseminated quartz-biotite assemblages. Epidote is often associated with zircon and allanite grains, occasionally also with molybdenite. Enrichment of epidote is observed at the boundary zone, where a lamellar K-Fe-Mn-Mg-Ba-silicate was also found, possibly hisingerite (Fig. 6.37 left), which could be an alteration product of the minerals of the lens shaped inclusion. This lens consists mainly of zoned, Ba-containing potassic feldspar (orthoclase), Fe-Mg micas (biotite) and epidote (Fig. 6.37 right).
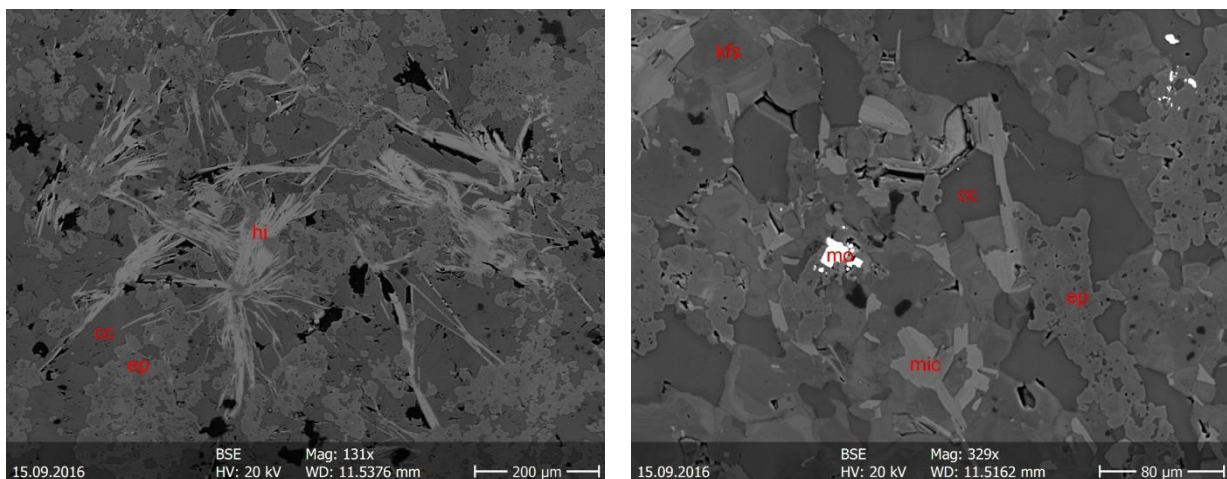
Figure 6.37 Left: flakes of a lamellar silicate mineral (hi: hisingerite?) in calcite (cc) – epidote (ep) matrix, dark patches are voids. Right: molybdenite (mo) in calcite (cc), epidote (ep), potassic feldspar (kfs) and mica (mic). Zonation of the feldspars is due to variable barium content.

Sample 12

The sample is a dolostone with iron oxide and sulphide mineralization. Main ore minerals are pyrite, magnetite and hematite, together in patches within the carbonate texture (Fig. 6.38 left). Minor chalcopyrite is also present, typically as small crystals of 10–20 μm, in some cases densely disseminated within an iron oxide grain. Mg-dominant ankerite and barite were found in fissures or veins (Fig. 6.37 right), Bi-telluride (tetradimite?) and sphalerite were found as inclusions of magnetite.

Figure 6.38 Left: Minerals in the order of brightness: chalcopyrite (cpy, small grains), pyrite (py), magnetite (mag), hematite (hem),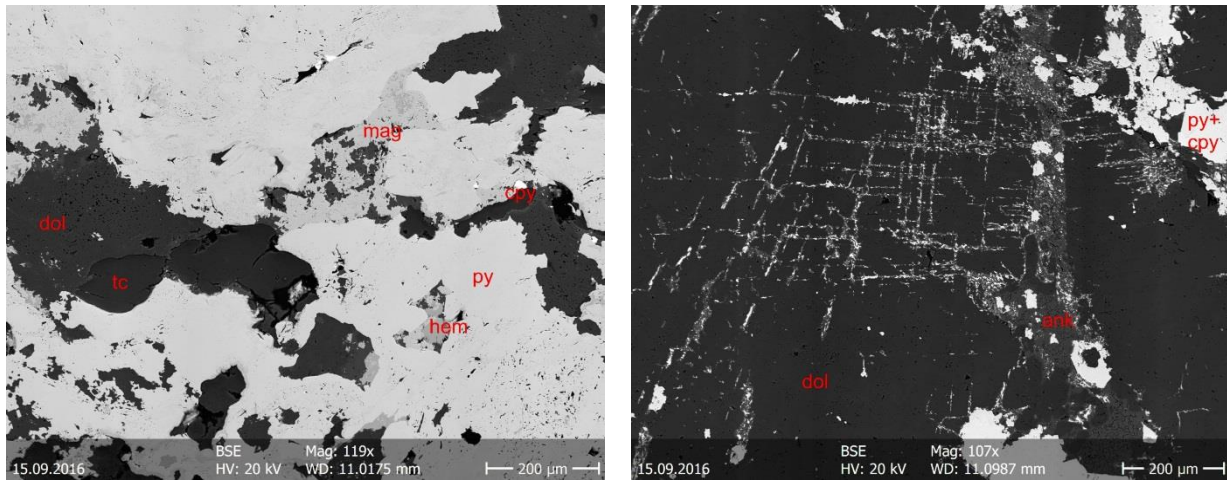 dolomite (dol) and talc (tc); Right: sulphide veins in fissures (along cleavage) of dolomite, a vein of Fe-Mg carbonate (ankerite, ank) is also visible. Bright patches are pyrite and chalcopyrite (py+cpy).

Sample 13

The sample consists of diopside and garnet as host rock for iron oxide and sulphide mineralization similar to that in sample 12. Pyrite seems to have grown in more than one generation, having twofold appearance (a massive and a spongy type), but without measurable differences in composition (Fig. 6.39). Small chalcopyrite and Bi-telluride grains were found, and a μm sized native gold grain in pyrite as well.
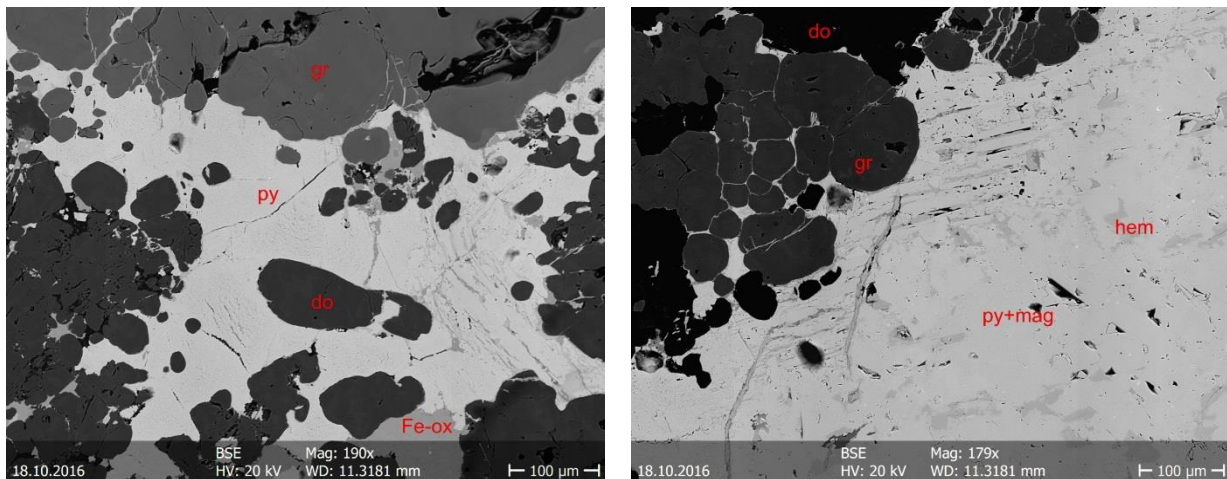
Figure 6.39 Left: Pyrite (py) and iron oxide (hematite) fills the space between garnet (gr) and diopside (do) assemblages. Right: boundary of the ore mineral assemblage zone (same area as on Fig. 6.20 right). Pyrite (py) and magnetite (mag) cannot be distinguished, hematite (hem) is darker. Garnet (gr) and diopside (do) at the boundary.

Sample 17

The rock consists mainly of cracked diopside, the cracks being filled with fluorite, lizardite and talc (Fig. 6.40 left). The spacing of the fissure net is of 0.1 mm magnitude, the fissure filling veinlets are 20–30 μm thick. Occasionally sphalerite, galena and molybdenite grains were also found in it. In a nest of some mm in diameter Pb-Bi-Cu sulphosalts of the aikinite-bismuthinite series were found embedded in serpentinite, associated with some small grains of galena and Ag-telluride at the rim of the diopside (Fig. 6.40 right).

Figure 6.40 Left: diopside (do) matrix with fissure-filling fluorite (fl), lizardite (li) and talc (tc). Right: aikinite (ai) in serpentinite, a nest within diopside (do) matrix.

Sample 18

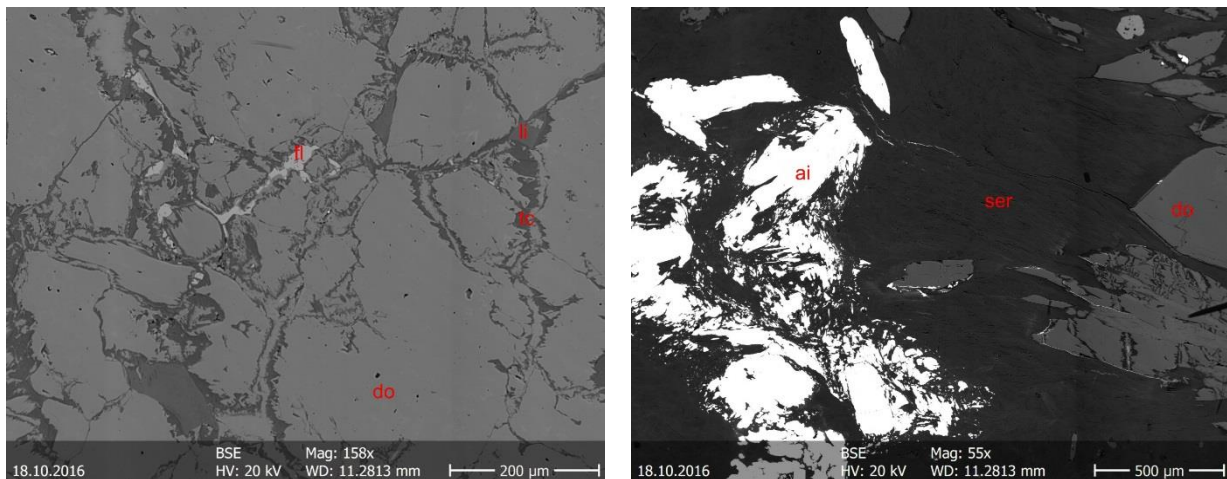In this sample calcite matrix embeds rounded grains of lizardite, grains consisting of mixed calcite and lizardite (possibly pseudomorphosa of precursor minerals) and acicular assemblages of szaibelyite (Fig. 6.41). Typical accessories are the Ti–REE(–Zr) oxides, in many cases having the same habit as the szaibelyite (possibly replacing it), but always in calcite. Szaibelyite can be also replaced by iron oxide in some stacks.
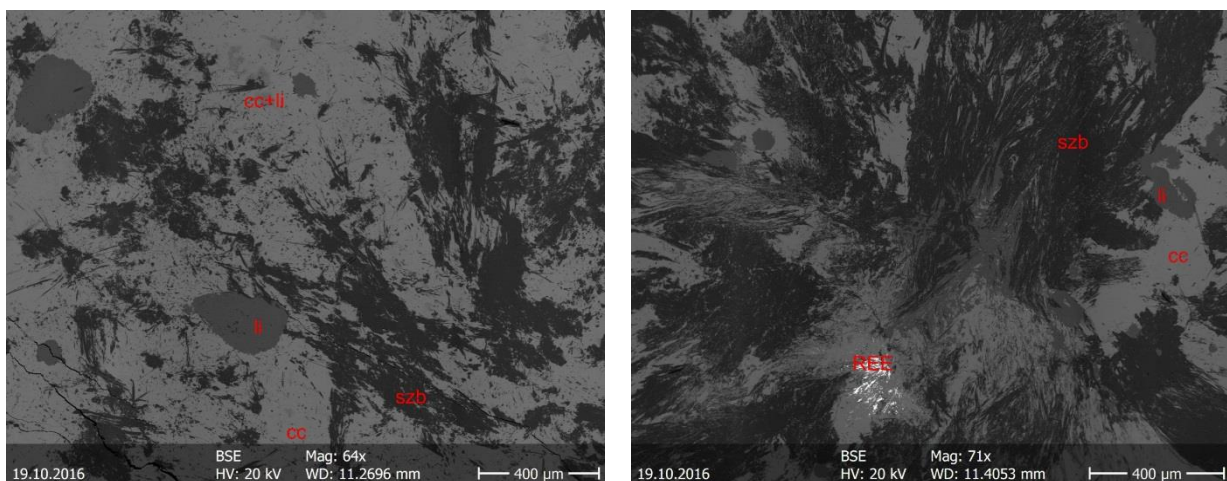
Figure 6.41 Left: calcite (cc) matrix with lizardite (li), grains comprising calcite and lizardite (cc+li) and acicular szaibelyite (szb). Right: Szaibelyite (szb) and Ti-REE oxides (REE) in calcite (cc) and lizardite (li).

Sample 20

This sample comprises large stacks of pyrite, sphalerite and chalcopyrite, the grain size exceeding 1 mm. The non-sulphide rock matrix consists of chlorite, potassic feldspar and quartz (Fig. 6.42). Chalcopyrite and sphalerite occurs together, typically grown over cracked pyrite or rims of pyrite crystals, but sphalerite also appears as round inclusion in pyrite, and chalcopyrite also appears within quartz matrix or on rim of quartz grains in chlorite. Typical accessories of chlorite are Ti-oxides and monazite (or, rarely, xenotime) in assemblages of some 10 µm, together with small zircon inclusions. Galena and molybdenite occur also in chlorite, sometimes with pyrite. Small silver minerals in chalcopyrite and Bi-telluride within pyrite were also found.
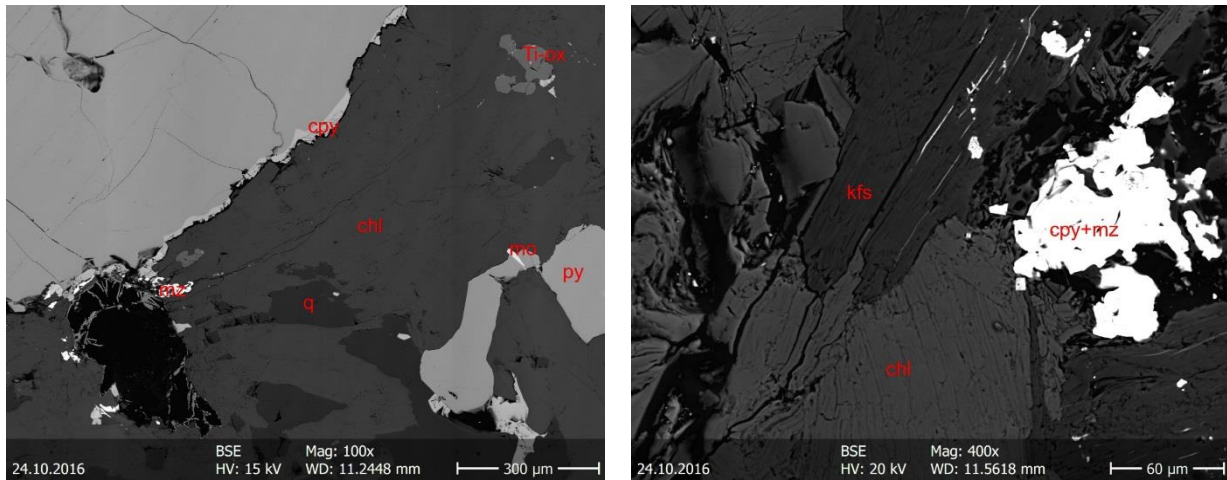
Figure 6.42 Left: pyrite (py) with chalcopyrite (cpy) on the edges and molybdenite (mo) in chlorite (chl) and quartz (q). The black patch is a void with monazite (mz) assemblages at the edges. Right: potassic feldspar (kfs) and chlorite (chl) with a chalcopyrite-monazite assemblage (cpy+mz). Bright fissures of the feldspar are filled by pyrite.

Sample 26

This massive sulphide ore consists almost exclusively of chalcopyrite, pyrite, sphalerite and cassiterite. The texture is banded. The differences are the proportions of the ore minerals and the grain size (Fig. 6.43). The size varies between 1 and 100 μm from band to band, but the magnitude is the same inside each band for all four coprecipitated ore minerals. In some sites there are more than one generations of these: cracks of sphalerite filled with pyrite, or cracks of large sized pyrite grains filled with chalcopyrite and sphalerite enclosing cassiterite grains. Occasionally 1–10 μm scale galena and tetrahedrite were also observed.

Figure 6.43 Left: banded texture with pyrite (py, chalcopyrite (cpy), sphalerite (sph) and cassiterite (ct). Right: Cassiterite (ct) enriched band in pyrite (py, chalcopyrite (cpy) and sphalerite (sph).

7 CHPM-relevant evaluation of the material testing results

7.1 Limitations of the sampling

When an evaluation has to be made from the results summarized in chapter 6, it is very important to consider the given conditions and limitations of the sampling which determine the relevancy of any conclusion. These limitations are discussed in the followings:
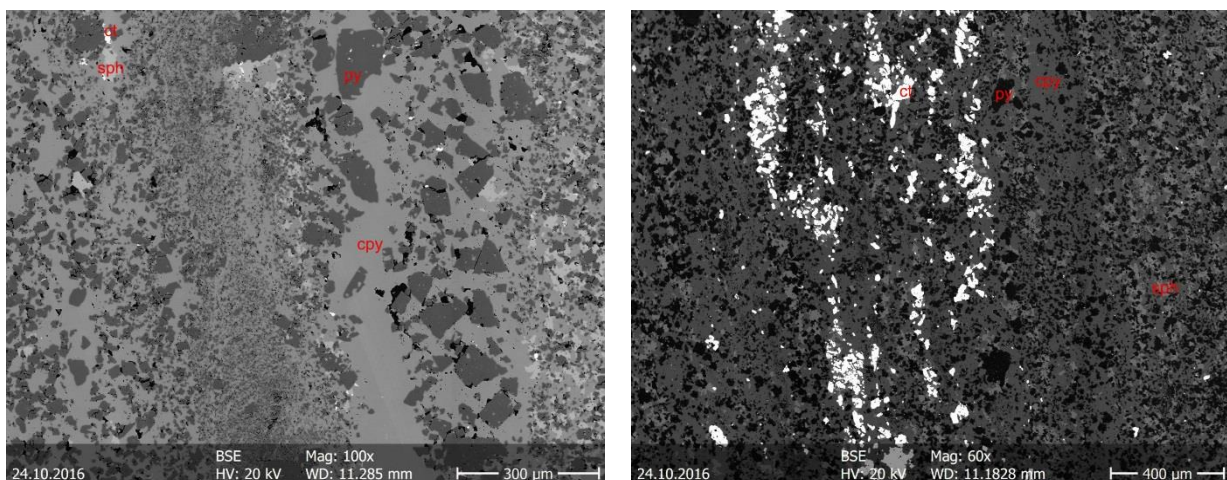
1. *Sampling was targeted on known ore bodies.* Ore in this context means raw material for traditional mining and processing with appropriate enrichment of ore minerals in any host rock. These bodies are rather inhomogeneous, and the spatial extension of the high-grade parts may be small within low grade matrix. Ore samples were taken mostly from high grade parts, with respect to the enrichment of visible (>0.1 mm size) ore minerals, typically sulphides and oxides. In some cases, additional samples represent the country rocks. When an EGS project is realized, it is very probable that – even if an ore body is hit – fluid flow will penetrate and leached material will come from a large volume of low grade material (not considered as ore in a traditional mineral resource prospecting) with a small contribution of high grade ores. For leaching experiments, however, it is best to start with small amounts of high grade materials to obtain measurable results.

2. *Sampling was made on surface outcrops or on material coming from shallow levels not corresponding to the typical depth of an EGS project.* Firstly, most mineralization processes produce zoned mineral assemblages and rock alterations, and hydrothermal processes require given pressure–temperature conditions existing at distinct shallow crustal levels. Tectonic processes, subsidence and burial (or uplift and exhumation) may transfer any ore type to the depth appropriate for an EGS project, but in that case one can reckon with progressive alteration of the ore and the rock forming minerals and the structure of the rock as well. Secondly, outcropping material is also subject of an alteration called weathering, an oxidative process in a medium of meteoric water typically, which changes the mineralogical and chemical composition of the rock. However, weathering can be regarded as a low temperature equivalent of the alteration caused by the leaching during the pumping of an oxidative fluid, therefore weathered samples may resemble to a subsequent state of the rocks affected by a working EGS project.

3. *The number of the samples is small.* Although the samples were taken as 'typical' for certain deposits, these are in no way representative either for the deposit type or for the mineralized area. A sample set bigger by one or two magnitudes would be required even for characterizing a single deposit when grade, structure and complex mineralogy are studied. On the other hand, rock forming and typical ore minerals (without quantitative evaluation), which will likely determine the composition of a fluid penetrating the rock, can be found in these hand-picked rock pieces already.

4. *Samples represent areas, ore and rock types picked out previously.* In the proposal of the CHPM project four test areas were delineated. All of these areas have their characteristic metallogeny, which does not cover the possible multitude of any deposit types. A majority of the samples (most of those from the Banatitic Magmatic and Metallogenic Belt and Sweden) comes from skarn deposits. This is a very significant ore type from our point of view, because it develops in carbonate rocks contactized by magmatic intrusions which may be ideal targets for EGS projects with regard to spatial extensions, depth level and permeability as well. A further group (including those from the Cornubian Ore Field) represents situations where the original host rock is not carbonate, but still the ores are related to intrusive or volcanic bodies. A single ore sample (supplemented with 3 country

rock samples) from the Iberian Pyrite Belt represents the stratiform ores, namely the VMS type. One stratabound, sediment-hosted ore type was involved from Hungary only; other stratiform ores, black shales are missing from the sample set.

5. *Samples do not contain information on structure of the rock body.* Pieces of rock chosen for cutting and making sections are cohesive blocks without any open joints and fractures. Besides the intact part, systematic joint sets or broken fault zones may exist and control the fluid flow. Mechanical properties and permeability of these blocks are not equal with those of the large-scale rock body.

7.2   Composition of the samples

As one of the aims of WP1 is to identify and characterize the ore types which are relevant for the CHPM technology, the samples are grouped accordingly and a short overview is given on the most important minerals and metals found in them (Table 7.1).

Id	Site	Ore type	Country rock / gangue minerals	Ore / accessory minerals
1	Baita Bihor	Skarn, sulphide molybdenum ore	*silicate* (gr): Mg, Fe *carbonate*: Ca	*phosphate*: Ca, Y *sulphide*: Mo
2, 18	Pietroasa	Skarn, borate	*carbonate*: Ca, Mg *silicate* (py, amph, gr): Ca, Mg, Fe	*borate*: Mg *oxide*: Fe
15, 16	Budureasa, Pietroasa	Skarn, magnetite	*carbonate*: Ca, Mg, Fe *silicate* (amph): Ca, Mg	*fluoride*: Ca *oxide*: Fe, Mn
17	Baita Rosie	Skarn, sulphide polymetallic ore	*silicate* (py): Ca, Mg, Fe	*fluoride*: Ca *sulphide*: Pb, Zn, Mo, Bi, Cu
12, 13, 14	Cacova Ierii, Baisoara	Skarn, magnetite and sulphide Cu ore	*carbonate*: Ca, Mg *silicate* (gr, amph): Ca, Mg, Fe	*oxide: Fe* *sulphide*: Fe, Cu
9, 10, 11	Dannemora	Skarn, magnetite	*carbonate*: Ca *silicate* (q, Kfs, mica, ep): Ca, K, Mg, Ba	*oxide*: Fe, Mn, Ti, Nb *sulphide*: Fe *silicate*: Zr, REE
19	Malmberget	Skarn, magnetite	–	*oxide*: Fe, Ti, V
20, 21	Kristinebergs-gruvan	Porphyry, sulphide Cu-Zn ore	*silicate* (q, chl): Si, Mg, Fe	*phosphate*: Ca, REE *oxide*: Fe, Cr, Co, Ti *sulphide*: Fe, Cu, Zn
7, 8	Craddock Moor, Herod's Foot	Porphyry and vein, sulphide Cu-Pb ore	*silicate* (q): Si	*oxide*: Fe, Ti, Nb *sulphide*: Fe, Pb, Cu, As
3	Gyöngyösoroszi	Vein, sulphide Pb-Zn ore	*carbonate*: Ca, Mg, Mn, Fe	*sulphide*: Fe, Zn, As, Cu, Pb
5, 6	Recsk	Porphyry and skarn, sulphide polymetallic ore	*silicate* (amph, gr): Ca, Mg, Fe	*oxide*: Fe, Cr, Co, Ni *sulphide*: Fe, Cu, Zn, Pb, Mo
4	Rudabánya	MVT Pb-Zn ore	*carbonate*: Ca, Mg, Fe, Sr *sulphate*: Ba	*sulphide*: Fe, Zn, Pb, Sb, As *oxide*: Fe, Zn, Pb (secondary)
23, 24, 25, 26	Porto de Mel, Corvo inferior	VMS Cu-Zn-Sn ore	*silicate* (q, fs, mica, chl): Ca, Mg, Fe, K, Na *carbonate*: Ca	*phosphate*: Ca, REE *oxide*: Sn, Fe, Ti *sulphide*: Fe, Cu, Zn

Table 7.1 Major mineral components and metals/metalloids of the samples. Samples are grouped according to the type of ore mineralization they represent

In Table 7.1 not only the most common metals are indicated, but several others which are present in relatively high concentration compared to their common abundance. When dealing with compositional data, not only the most abundant rock forming and ore minerals, but accessories are also important. Accessories, alteration products not linked directly to the ore formation but enriched in a larger rock volume may represent a quantity of similar magnitude as the ore minerals themselves. Some of the samples can be regarded as a connected group, so these are mentioned together; others have special properties.

The main characteristics of the samples are summarized below:

Samples representing skarn mineralization:

<u>Sample 1</u> is a single-sulphide ore of molybdenite, representing a special deposit type not common in the BMMB. Iron is bound to silicate minerals and not to sulphides or oxides. High phosphorous concentration indicates the presence of phosphate minerals, possibly apatite and some Y- and REE-containing phases, which were not identified, with a grain size of µm-scale.

<u>Samples 2 and 18</u> represent another special and not common deposit type of the BMMB, comprising mainly Mg-borates in carbonate-silicate matrix. Calcite is abundant. Fe and S content is low, sulphide minerals are missing, oxides-hydroxides are subordinate (probably weathering products in the samples only).

<u>Samples 15 and 16</u> are iron oxide ores with carbonate country rocks of a common deposit type, representing a situation where sulphide minerals are missing. While sample 15 represents almost pure Fe-Mg-oxides, sample 16 is dominated by the carbonate matrix and a high fluorite content.

<u>Sample 17</u> has a silicate matrix and base metal sulphide minerals (mainly sulphosalts) hosted by it. The speciality of the situation lies again in the presence of fluorite in veins crosscutting the matrix.

<u>Samples 12, 13 and 14</u> represent a common deposit type of iron oxides combined with iron and minor copper sulphides hosted by skarn rocks. Magnetite and pyrite occur in very close connection to each other. The matrix of sample 12 is carbonate, matrices of samples 13 and 14 are silicate dominated.

<u>Samples 9, 10 and 11</u> together represent a deposit comprising iron oxide and minor iron sulphide (sample 10), and the host rocks are metamorphic (samples 9 and 11), both with carbonate and silicate minerals. Barium content of the silicate rock forming minerals and presence of Ti-oxides and attached HFSE bearing minerals are significant characteristics.

<u>Sample 19</u> is iron oxide with some titanium content from a skarn deposit. Carbonates and sulphides are missing, silicates are subordinate.

Samples representing porphyry and vein-type mineralization:

<u>Samples 20 and 21</u> represent a common situation where quartz dominated silicate matrix (sample 20) or almost pure quartz matrix (sample 21) contains iron, copper and zinc sulphide minerals (while lead is subordinate), also iron oxides in sample 21. Carbonates are missing. Ti-oxides and REE-phosphates of small grain size were found as common accessories.

<u>Samples 7 and 8</u> are quartz hosted iron, copper, lead sulphides (also arsenic sulphides in sample 7) with subordinate zinc. This is a similar situation as in the previous case with a switch between lead and zinc, sphalerite and galena. Iron and titanium oxides are also present, and titanium oxides also incorporate some niobium. Carbonates are missing.

<u>Samples 5 and 6</u> represent quartz-hosted (sample 5) and massive (sample 6) iron oxide and iron and copper sulphide mineralization with significant contribution of lead, zinc and molybdenum. This is the rich

polymetallic variation of the quartz-hosted sulphide ores. Oxides also incorporate some chromium and nickel.

Sample 3 is a carbonate vein hosting polymetallic (iron, zinc, arsenic and lead) sulphides (copper is subordinate). Silicates are not typical.

Sample representing MVT-type mineralization:

Sample 4 represent a special deposit type of barite hosted iron, lead and zinc sulphides, with significant bismuth content and with secondary oxide-hydroxide phases. Carbonates and silicates are also present in minor quantity.

Samples representing VMS mineralization:

Samples 23, 24 and 25 represent volcanic host rocks of the massive iron, copper, zinc sulphide and tin oxide ore of sample 26. The deposit is special in some characteristics (like the cassiterite content), but it can be regarded as common in the Iberian Pyrite Belt. The silicate rocks also contain iron and copper sulphide or iron oxide grains and a significant amount of phosphates (also REE phosphates) as accessories.

The described sample set provides an opportunity for testing of several compositional variations, both of common and special properties:

- carbonate hosted iron-rich oxide mineralization;

- carbonate hosted iron-rich oxide and sulphide mineralization with or without base metals;

- carbonate hosted base metal sulphide mineralization;

- silicate/quartz hosted sulphide mineralization with different base metal assemblages;

- silicate hosted iron-rich oxide mineralization;

- borate, phosphate and fluorite containing mineralization;

- single-sulphide (molybdenite) mineralization;

- barite-hosted sulphide mineralization.

7.3 Role of mineralogy and deposit type in planning the CHPM technology

The mineral information should be used to engineer proper leaching fluids. It could be searched if there is a possibility to couple the useful target minerals/elements with particles, minerals having electric/magnetic properties, or give selectively the target minerals proper surface coating to make them separable from the rest of the components.

It is highly probable that, beyond useful metals, other elements will get into solution in relatively high concentration, like arsenic from sulphides or barium from feldspars. Excess mobilization of iron, calcium and magnesium should also be envisaged. These elements all have to be processed. Some of the co-liberated mineral components, like fluorine, might be extremely aggressive chemicals contributing to the decomposition of minerals which would be stable otherwise, and causing heavy corrosion of pipes and equipment.

Textural properties are likely to play an important role during leaching of the rocks. In a heterogeneous mineral assemblage different elements have not equal reaction speeds not only depending on chemical and crystallographic structure, but also on grain size and habit. Anisometric (lamellar and acicular) and small grains have larger specific surface area compared to isometric and large ones, therefore these may react

faster. A temporal change of the solution can also be envisaged, as composition of the rock and fluid flow paths are changing due to the fluid-rock interaction during leaching.

As for the ore deposit type, from technological aspects the skarns are preferable targets since (at least at near surface conditions) their carbonate matrix can be dissolved relatively easily, while the relatively stable silicate minerals remain almost intact and may act as proppants, while dissolved carbonates produce secondary permeability enlarging the reactive surface of the minerals. In the pressure-temperature range expected in an EGS project this stability relation might alter, but it remains still probable that carbonates, in contrast with silicates will be dissolved without significant insoluble residue.

8 Methodology for the petrophysical tests

8.1 Introduction to the description of methodology

During the research work outlined in Task 1.3, the characteristics of potential deep ore bodies relevant to common heat and metal extraction are investigated. These investigations have included ore mineralogy, texture and geochemical characterization, which may lead to a realistic interpretation of the thermal properties, fluid and heat flow characteristics.

In the following phase of the project, within Task 2.1, the different petrophysical characteristics will also be tested, experiments will be carried out on the samples, and this may lead to the better understanding of rock stresses and their impact on fracture formation in the target test sites. In the present report, only the methods for these petrophysical are selected and briefly described. The planned tests are fractal simulation technique, acoustic tests under tri-axial load, and tri-axial strength measurements of the samples. The mineralogical and petrological features clarified in Task 1.3 will serve as an input for the petrophysical tests. For these tests, samples will be selected from those which were used in Task 1.3.

Knowledge on petrophysical conditions and rock parameters is needed for planning the CHPM technology, in order to know if sufficient permeability is available for the in-situ application of leaching.

The importance of petrophysical parameters has several aspects:

- The most economic way to obtain information about rocks in unexplored depth is using geophysical techniques – these techniques require measured petrophysical parameters of the forecasted lithologies during evaluation.

- To access the target lithologies at the planned depth, a secure and efficient drilling technology has to be used, and its design is based on petrophysical parameters.

- To leach orebodies at the planned depth, microfractures should be enhanced or reopened and maintained – this requires detailed knowledge of rock stresses and rock strength.

Since samples from the target geologies and the target depths are very scarce or not available, we will apply various indirect methods:

- Petrophysical information learned from deep drilling programs;

- Fractal geometric simulation of fracture propagation;

- Acoustic tests at elevated pressure on surface samples;

- Rock mechanical tests on surface samples.

These indirect approaches necessarily bring several drawbacks to the modelling:

- Surface samples are de-stressed; their state is markedly different from their deep counterparts;

- Surface orebodies are affected by oxidation and weathering; their mineralogy is not alike that of the in-situ orebodies at depth;

- Time cannot be modelled, i.e. neither the pressure, nor temperature and material flows can be modelled in laboratory for the time analogous to geological processes, which may be active at great depth in virgin terrains.

These inevitable weaknesses should be considered when creating these models and using them for planning.

8.2 Parameters influencing the application of CHPM technology; selection and setup of possible laboratory testing methods

In our view the EGS technology requires the existence of a fracture system. The spatial distribution of the fractures principally depends upon two main factors: (1) the primary stress state and (2) the pre-existing fractures.

The direction and the relative size of the primary main stresses define the direction of the resulting fractures. However, the main stress directions are not obligatorily coincident with the largest vertical and the smallest horizontal stress directions. This approximation is however acceptable, because most measurements take place in drillholes, where the largest main stress has vertical direction.

An existing fracture is easier to reopen than to create a new fracture. The difference of the two pressure values (one of fracking and the other of re-opening a pre-existing fracture) is equal with the tensile strength of the rock. With increasing depth the tensile strength becomes smaller than the primary stresses of the rock-body. It means, that at greater depths the influence of the pre-existing fractures diminishes.

8.3 Petrophysical Information learned from deep drilling programs

Most analogous information for planned works should come from previous experience of deep scientific drilling programmes. The deep scientific drilling in different countries is now globally registered, published and made partially investigable under the umbrella of ICDP – International Continental Scientific Drilling Program (http://www.icdp-online.org/).

Although the ICDP projects do not especially aim at mineral exploration or commercial extraction of elements, some of the drillholes were planned and some of them completed on mineralized regions throughout the world, and their finding should be incorporated in our further research and design works. Without going into details of the results, the realized European deep scientific drilling programs are summarised in Table 8.1.

Locality	Country	Drillhole ID	Max depth (m)	Year	Reference
Krafla	Iceland	IDDP-2	2,210	2009	Ármansson et al (2014)
Are	Sweden	COSC-1	2,497	2014-	Lorenz et al (2015)
Outukumpu	Finland		2,516	2004-2010	Kukkonen (2011)
Kola	Russia	KSDB	12,566	1970-1994	RAS (1998)
Bayreuth	Germany	KTB-1	10,000	1994	Emmermann et al 1997

Table 8.1 Realized deep scientific drilling programs in Europe.

To characterize the magnitude of petrophysical problems encountered, the summary results of the Outukumpu drillhole is cited here (Kukkonen et al 2011): From this borehole 1992 core samples were taken and subjected to petrophysical laboratory measurements of the at the Geophysical Laboratory of the Geological Survey of Finland (GTK). Sampling was approximately at one meter intervals. Density and porosity,

magnetic susceptibility and the intensity of remanent magnetization, electrical properties (resistivity and chargeability), P-wave velocity and thermal conductivity were determined.

They concluded that the depth along the drill core and the density or susceptibility of cores have got no systematic relationship. P-wave velocity and specific resistivity tend to decrease with depth. The porosity of mica schists increases with depth, but the drill core bulk densities do not change. Microfracturing due to pressure release possibly explains part of this effect. Remanent magnetization in black shales decreases compared to the surface – it is explained by changes in the pyrrhotite structure. Drilling results could be used to calibrate the seismic survey results of further 15 commercial ore exploration programs (Airo et al 2011).

This and many other well-published information should be screened, reviewed and interpreted with the special objective outlined in the CHPM H2030.

8.4   Fractal geometric simulation of fracture propagation

Investigations of the spatial distributions of fracture networks in fractured rock bodies are essential for accurately understanding fluid flow within, and storage capacity of, reservoir rock masses.

Given that the porosity of the matrix in fractured hard rock bodies (igneous, metamorphic or carbonate) is usually negligible, the spatial distributions and behaviour of individual fracture clusters are essential, as subsurface fluids are mostly linked to the fracture network within the rock. Because several fracture networks can coexist in fractured reservoirs without any actual communication occurring between them, identifying and analyzing communicating clusters in detail within the whole fracture system is particularly important. This is hampered by the fact that hydraulically active fracture clusters are generally beyond the resolution of high-scale seismic and low-scale well-log and microstructural studies.

Due to the subsequent deformation events that occur in rock bodies, the size distribution of individual fractures is relatively wide, ranging from sub-microscopic to several hundred meters in scale. However, certain characteristic parameters of the individual fractures are comparable between different scales, enabling detailed mathematical modelling of the fracture clusters based on parameters gained at a given scale by detailed analysis of the rock body. The main goal of such simulations is to develop a three-dimensional model of the fracture network of the rock body at the scale of the entire reservoir, based on observed lithological parameters and the inferred structural evolution history. A detailed investigation of the modelled fracture network can help us to gain a better understanding of the hydrodynamic parameters of the reservoir.

One of the most important descriptive parameters of fractures is their length, or in three dimensions using the disk model, the diameters of the disks. Several studies have described the size distribution of fractures of a given generation. There is a general agreement that the size distribution of fracture lengths is usually highly asymmetric; the number of small fractures significantly overwhelms the number of large ones.

In contrast to the length and aperture, where definitions are relatively straightforward, spatial density of fractures is an attribute that has been defined in several ways due to theoretical considerations. It has been systematically proven by empirical data that fracture networks behave geometrically as fractal-like objects, regardless of the lithological parameters or the structural evolution of the rock body. This enables a complex analysis of the disks representing discrete fractures, specifically in terms of their size (diameter, aperture) and spatial distribution at a given scale. The spatial distribution of the midpoints of fractures has been analysed with regards to scale; the fractal dimension is used as a proxy to describe the density of midpoints. This is accomplished by an algorithm known as box-counting.

In the simulation, we rely on the fractal nature of the studied pattern when comparing densities at different scales. The spatial distribution of fractures, if they behave as fractals, is the same at all scales.

REPSIM code (M. Tóth et al. 2004) is one of the fracture network modelling tools that use the fractal geometry-based DFN method. Accordingly, the set of disks representing discrete fractures are generated using the following recursive algorithm:

1. The studied area is subdivided into grid blocks of homogenous properties (generator elements);

2. Blocks received at step i are subdivided into n ($\in N$) further blocks yielding $n3$ blocks of equal size (r/n);

3. Based on the fractal dimension calculated for the given generator elements ($N(r) = r -D$), the smaller blocks containing the central points of the fractures are randomly selected;

4. Steps 2 and 3 are recursively repeated;

5. When a given threshold value is reached, the centres of blocks containing fractures represent the centres of the fractures (fracture seeds);

6. From the given distributions, randomly chosen parameters (length and orientation) are used to create the disks around the fracture centres;

7. Using (2), aperture is calculated for each individual fracture (M. Tóth and Vass 2011).

8.5 Acoustic testing methods

The acoustic laboratory of the Department of Geophysics, University of Miskolc is equipped with a digitally controlled test system including 2-channel ultrasonic testing device, a triaxial pressure cell and a load frame for the uniaxial load of the samples. The measurements can be carried out on cylindrical samples with diameter 35 mm and length 80-120 mm. It is required that the endcaps of the samples are parallel and smooth cut.

For the determination of the longitudinal (P) and transverse (S) wave velocities the pulse transmission technique (Toksöz et al. 1979) is used. The samples are placed between the pressure stamps of the triaxial cell, which includes the two pairs of piezoelectric crystals. Transducers in the stamps have 1 MHz eigenfrequency and are sealed against the confining pressure.

The pressure cell enables triaxial loading ($\sigma_1 \neq \sigma_2 = \sigma_3$), maximum 300 kN force in axial direction and 80 MPa confining pressure onto the mantle of the sample. The pulse generator of the ultrasonic 2-channel testing device transmits a voltage pulse (run time 10 ns) which starts acoustic waves in the rock sample. The receivers transform these acoustic signals to voltage pulses. The arrival times of the pulse can be detected by the software GMuG/GL Test Systems PCUSpro, i.e. from the length of the sample it is possible to calculate P and S wave velocities.

The signal quality depends on the properties of the rock, i.e. in very porous and/or coarse grained rock measurement can be difficult (especially for S waves in wetted rocks, because S waves cannot physically propagate in liquids).

We perform measurements under varying uniaxial stresses within the Freely Programmable Interface module of the software DION 7. The uniaxial load is increased stepwise from the required minimal load up to the maximal one. On the plateaus, equilibration times are embedded for the relaxation of the samples. At the end of each plateaus the P and S wave velocities are determined. We apply 256-fold stacking to increase

the signal-to-noise ratio. After reaching the last measurement point, the load is decreased stepwise and the velocities are determined similarly. With these measurements, the acoustic hysteretic behaviour of the samples can be studied, which provide information about the speed of reopening of microcracks (qualitatively) and the accidental making of new microcracks.

A rock physical model was developed at the Department of Geophysics for the description of pressure dependence of acoustic velocities. According to the model, the velocity data (α and β are the P and S wave velocities, respectively) measured at different pressures (σ) are processed in joint inversion procedure, where the direct problem is defined by the following equations:

$$\alpha = \alpha_0 + \Delta\alpha_0 \, (\, 1 - exp(-\lambda_V \sigma \,)) \, , \quad \beta = \beta_0 + \Delta\beta_0 \, (\, 1 - exp(-\lambda_V \sigma \,)) \, .$$

After determining the model parameters (α_0, β_0) P and S wave velocities at $\sigma = 0$, $\Delta\alpha_0$, $\Delta\beta_0$ - the P and S wave velocity drops, i.e. the velocity differences between maximal and zero stresses, λ_V - rock physical parameter, the logarithmic stress sensitivity of velocity drops), the P and S wave velocities can be calculated for any uniaxial pressure of interest. If pressure dependent P and S wave velocities are available, and the density of the sample is known, dynamic elastic moduli can be determined: compression (bulk) moduli (K), shear moduli (= first Lamé parameter, μ), Young's moduli (E), second Lamé parameter (λ):

$$K = \rho\left(\alpha^2 - \frac{4}{3}\beta^2 \right), \quad G = \mu = \beta^2\rho \, , \;\; E = \beta^2\rho\,\frac{3\alpha^2 - 4\beta^2}{\alpha^2 - \beta^2} \, , \;\; \lambda = \alpha^2\rho - 2\mu \, .$$

8.6 Rock strength measurements

For the measurements of strength and elastic properties of rock samples the equipment of the Mining Engineering Department of the University of Miskolc will be used:

- Hydraulic test loading machine up to 1000 kN loads

- Triaxial cell and hydraulic unit up to 300 bar confining pressure

- Cells for measuring load and displacement and QUANTUM-X data acquisition system produced by HBM (Hottinger Baldwin Messtechnik Gmbh)

- CATMAN software for data processing

The tests are standard, as recommended by the International Rock Mechanics Association (ISRM):

- Uniaxial compressive strength – according to Bieniawski, 1979;

- Triaxial compressive strength – according to Franklin, 1983;

- Indirect tensile strength by Brazil test – according to Bieniawski & Hawkes, 1978.

It should be noted that in laboratories, sample bodies formed from intact rock blocks are examined. Fractures in the rock body should be taken into account if real strength should be known. Numerous types of conditions of failure are published. Only the least and the highest main stress are taken into consideration by some methods and the middle value is neglected. These failure conditions can be illustrated in two dimensions as failure curves. If the middle main value is not neglected, three-dimensional failure surfaces are required for the illustration. The rock mass can be recognized to a limited extent; furthermore, standard deviation of the strength results is significant due to the

inhomogeneity of the rocks. In practice, it is satisfactory to consider only the lowest and highest main stresses and use failure curves, as inaccuracy of this method does not exceed inaccuracy resulted by inhomogeneity. Therefore, applicability of failure curves is proven by practice. Such criteria based on the Mohr failure condition are the Mohr-Coulomb yield line, parabolic and hyperbolic curves and the Hoek-Brown curve, as well.

It is a well-known fact that no linear curves may be applied in the whole range of stresses (compressive and pull stresses). Hoek-Brown curves are widely used nowadays for the determination of characteristics of cracked rock masses. The curve in question was modified several times and was adjusted to evaluated in situ observations can be described as follows:

$$\sigma_1 = \sigma_3 + \sigma_c \cdot \sqrt{m \cdot \frac{\sigma_3}{\sigma_c} + s}$$

,

where m and s are functions of rock quality and rock structure GSI (Geological Strength Index).

For laboratory tests

$$\sigma_1 = \sigma_3 + \sigma_c \cdot \sqrt{m_i \cdot \frac{\sigma_3}{\sigma_c} + 1}$$

,

where m_i is a value between 5 and 35 describing intact rock mass.

In the range of pull stresses and small compressive stresses, failure may well be described with parabolic curves but such curves yield no good approximation in the case of large compressive stresses. In this range, the correlation between normal and shear stresses is much more linear. All this led to the idea that it is suitable to apply a hyperbolic failure curve across the whole range of stresses.

The main advantage of the proposed process by is that every element is supported by measurement results. The conventional triaxial compressive strength of the rock is measured for uniaxial pull, uniaxial compression and different side pressures as many times as possible. The average values of the measurement results obtained in this way are plotted on the σ–τ plane (Mohr plane). Then, according to the well-known principles of function approximation, the hyperbolic failure curve best accommodated to measurement results is determined (Figure 8.1).
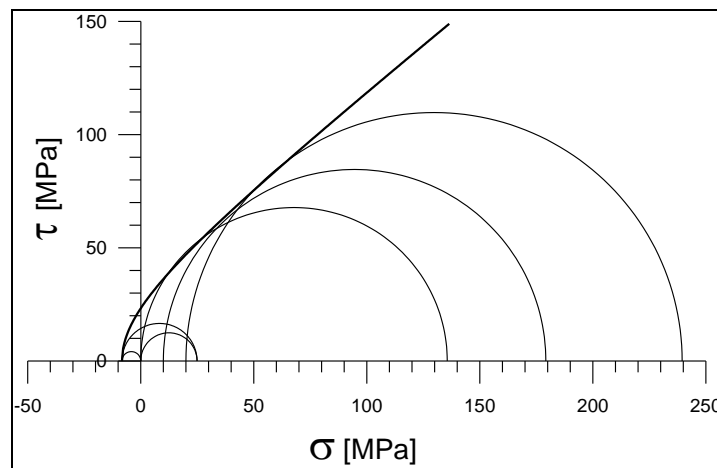

Figure 8.1 Hyperbolic curve best accommodated to measurement results (Debreczeni, 2012)

The recent information obtained from super-deep drillholes have revolutionized our knowledge regarding the prevailing stress conditions at great depth. As it is summarized from the results of the KTB drillholes, the

"stress magnitude profiles can be separated into the linear increase of individual stress components with depth (z) and the non-linear decrease of dimensionless stress ratios with depth (l/z) in agreement with simple elastic spherical shall models of the Earth's crust. At a greater depth, the range of the lateral stress coefficient k narrows considerably and below 4 km the observed values generally approach one, Heim's rule isotropic lithospheric stress is valid. At great depth, the lateral stress coefficient is smaller than one. Close to the surface of the Earth, horizontal stresses increase because the vertical stress decreases to zero at a free surface. Depending on the rock mass property, topography, erosion and tectonics near surface horizontal stresses can reach six times the vertical stress component" (Zang & Stephansson 2010).

For the smaller depths Hoek & Brown's (1980) model was widely accepted to predict stress developments with depth. The new KTB drillhole results have modified this view for depths greater than 3 kilometres (Figure 8.2).
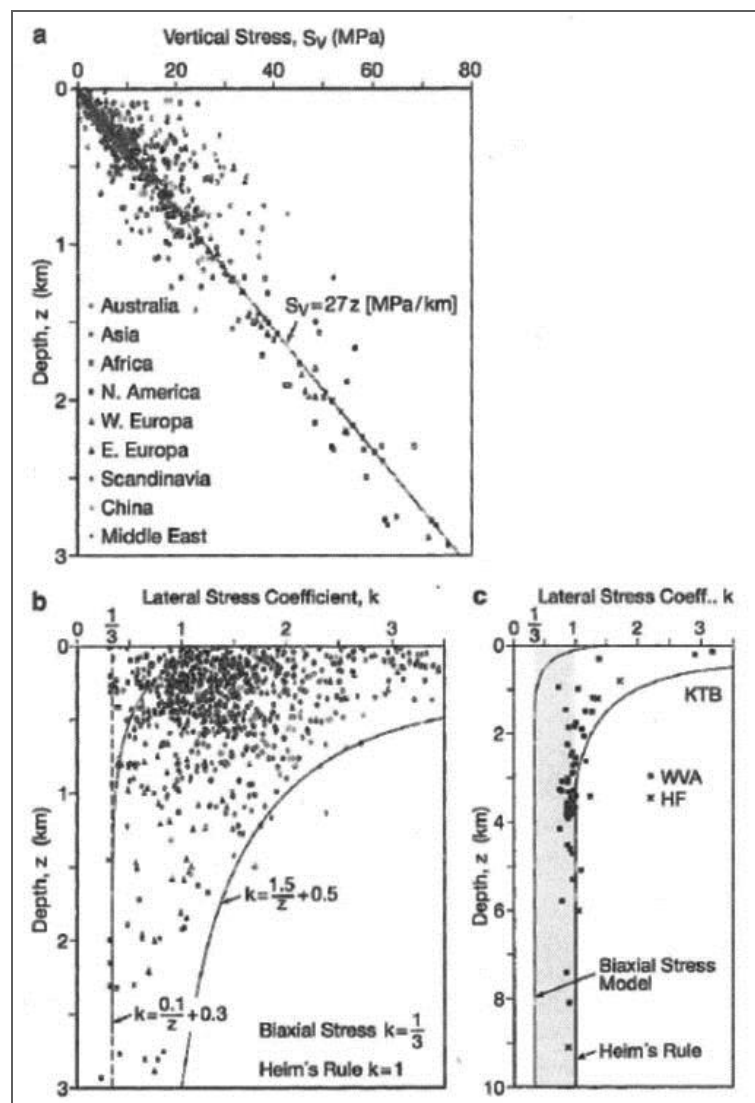

Figure 8.2 Vertical (a) and (b) horizontal (b) stress coefficients down to 3 km depths by Hoek and Brown (1980). The diagram (c) extends the depth to 9.1 km using the data obtained from the KTB drillhole.

Tri-axial strength tests are useful to model the in-situ stress conditions. Pre-existing fracturing has high influence on strength at near surface conditions, but lose their importance at 3-5 km depth. At greater depths, the tensile strength of the rock has decreasing influence on the failure of rocks, at 5 km depth the in-situ stress prevails irrespective of the rock strength properties.

9 Conclusions

The aim of this study is to collect mineralogical, petrographical and geochemical data about different ore types which can be potential targets of the CHPM applications. The methodology for the petrophysical laboratory examinations is also characterized. The results will provide input for the rock mechanical and the leaching tests, which will be carried out in Work package 2.

The examined rock and ore samples were collected mostly from the four study sites: The Cornubian Ore Field (England), the Banatitic Magmatic and Metallogenic Belt (Romania), the three mining districts of Sweden (Bergslagen, Skellefte and Northern Norrbotten), and the Iberian Pyrite Belt (Portugal). These samples were completed by further ones from Hungary so that more ore mineralization types should be represented. Altogether, 26 samples were studied.

The samples were analysed by X-ray diffraction, X-ray fluorescence spectrometry, polarisation microscopy and electron microprobe and EDX measurements. The mineralogical analysis was qualitative as the samples do not represent the ore grade of the deposits. Beside the identification of the mineralogical and geochemical components, the textural parameters were also examined. The results were assessed and summarized with grouping the samples into the following ore types: skarn, porphyry, vein-type, MVT and VMS deposits.

From the aspects of the CHPM technology, skarn mineralizations are preferable targets for multiply reasons. Their spatial extension and depth are in line with the requirements of the technology. The carbonate matrix is relatively easy to dissolve, increasing the permeability and the reactive surface of minerals for leaching, while the silicates remain intact and can serve as proppants. However, the technology can be developed in any rock type.

It is important to emphasize that there are several limitations of drawing general conclusions in relevancy with the CHPM technology from the examination results. The samples represent the high-grade parts of the ore deposits, while in the CHPM technology low-grade, extended ore bodies will be used. Furthermore, the number of the studied samples is small, and they do not represent the whole mineralized area they are from. The samples were taken from surface outcrops or from shallow depth while an EGS project established at a depth of several kilometres. It is also a problem that the samples do not provide information on the structural characteristics of the ore body.

In spite of these limitations, the study is a good base for the following phases of the project. The mineralogical-geochemical data will be used when the leaching tests will be planned and assessed on the same samples. The mineralogy will also be considered during the interpretation of the petrophysical experiments.

10 References

AIRO, M.L., SÄÄVUORI, H., VUORIAINEN, S. 2011: Petrophysical properties of the Outokumpu Deep Drill Core and the surrounding bedrock. *Geological Survey of Finland, Special Paper* **51**, 63–82.

ÁRMANNSSON, H., FRIDRIKSSON, T., GUDFINNSSON, G.H., ÓLAFSSON, M., ÓSKARSSON, F., THORBJÖRNSSON, D. 2014: IDDP-The chemistry of the IDDP-01 well fluids in relation to the geochemistry of the Krafla geothermal system. *Geothermics* **49**, 66-75. DOI:10.1016/j.geothermics.2013.08.005.

BIENIAWSKI, Z.T. AND HAWKES, I. 1978: Suggested methods for determining tensile strength of rock materials. *International Journal of Rock Mechanics and Mining Sciences & Geomechanics Abstracts*, **15**(3), 99-103.

BIENIAWSKI, Z.T. 1979: Suggested methods for determining the uniaxial compressive strength and deformability of rock materials. *International Journal of Rock Mechanics and Mining Sciences & Geomechanics Abstracts,* **16**(2), 135-140.

DEBRECZENI, Á. 2012: Some remarks on the failure curves of rocks, *Geosciences and Engineering,* **1**(1), 113-119.

EMMERMANN, R., ALTHAUS, E., GIESE, P., STÖCKHERT, B. (EDS.) 1997: KTB Hauptbohrung – Results of Geoscientific Investigation in the KTB Field Laboratory. Final Report: 0-9101 m. *KTB Report,* 95-2 (ISBN 3-928559-15-X)

FRANKLIN, J. A. 1983: Suggested methods for determining the strength of rock materials in triaxial compression: Revised version, *International Journal of Rock Mechanics and Mining Sciences & Geomechanics Abstracts*, **20**(6), 285-290.

HOEK E, & BROWN E.T. 1980: Empirical strength criterion for rock mass. *Journal of Geotechnical and Geoenvironmental Engineering,* **106**,1013-1035.

KUKKONEN, I.T. (ED.) 2011: Outokumpu Deep Drilling Project 2003–2010. *Geological Survey of Finland, Special Paper* **51**, 252 p.

LORENZ, H., ROSBERG, J.E., JUHLIN, C.; BJELM, L., ALMQVIST, B.S.G., BERTHET, T., CONZE, R., GEE, D.G., KLONOWSKA, I., PASCAL, C., PEDERSEN, K., ROBERTS, N.M.W., TSANG, C.F. 2015: Operational Report about Phase 1 of the Collisional Orogeny in the Scandinavian Caledonides scientific drilling project (COSC-1), 10.2312/ICDP.2015.002 GFZ *German Research Centre for Geosciences*

M. TÓTH, T., SZŰCS, É., SCHUBERT, F., HOLLÓS, CS. 2004: Conceptual fracture network model of the crystalline basement of the Szeghalom Dome (Pannonian Basin, SE Hungary). *Acta Geologica Hungarica* **47**(1), 19–34

M. TÓTH, T., VASS, I. 2011: Relationship Between the Geometric Parameters of Rock Fractures, the Size of Percolation Clusters and REV. Mathematical Geosciences **43**, 75–97 DOI 10.1007/s11004-010-9315-4

RAS – RUSSIAN ACADEMY OF SCIENCES 1998: Kola Superdeep; Scientific Results and Research Experience, Moscow 1998, Ministry of Natural Resources of the Russian Federation, *Russian Academy of Earth Sciences*

TOKSÖZ, M. N., JOHNSTON, D. H., TIMUR, A. 1979: Attenuation of seismic waves in dry and saturated rocks, I. Laboratory measurements. *Geophysics*, **44**(4), 681–690.

ULUSAY, R. (ED) 2015: The ISRM Suggested Methods for Rock Characterization, Testing and Monitoring: 2007-2014. 288 p. *Springer*, Heidelberg, New York.

ZANG, A., STEPHANSSON, O. 2010: Stress Field of the Earth's Crust. *Springer*, Dordrecht Heidelberg London New York. 324 p. ISBN 978-1-4020-8444-7, DOI 10.1007/978-1-4020-8444-7